

# Analytical and experimental performance evaluation of an integrated Si-photonic balanced coherent receiver in a colorless scenario

Mohamed Morsy-Osman,<sup>1,\*</sup> Mathieu Chagnon,<sup>1</sup> Xian Xu,<sup>1</sup> Qunbi Zhuge,<sup>1</sup> Michel Poulin,<sup>2</sup> Yves Painchaud,<sup>2</sup> Martin Pelletier,<sup>2</sup> Carl Paquet,<sup>2</sup> and David V. Plant<sup>1</sup>

<sup>1</sup>Department of Electrical and Computer Engineering, McGill University, Montréal, Québec H3A 2A7, Canada

<sup>2</sup>TeraXion, 2716 Einstein, Québec, Qc, G1P 4S8, Canada

\*mohamed.osman2@mail.mcgill.ca

**Abstract:** We study analytically and experimentally the performance limits of a Si-photonic (SiP) balanced coherent receiver (CRx) co-packaged with transimpedance amplifiers (TIAs) in a colorless WDM scheme. Firstly, the CRx architecture is depicted and characterization results are presented. Secondly, an analytical expression for the signal-to-noise ratio (SNR) at the CRx output is rigorously developed and various noise sources in the context of colorless reception are outlined. Thirdly, we study experimentally the system-level CRx performance in colorless reception of  $16 \times 112$  Gbps PDM-QPSK WDM channels. Using a 15.5 dBm local oscillator (LO) power, error free transmissions over 4800 and 4160 km at received powers of  $-3$  and  $-21$  dBm per channel, respectively, were achieved in a fully colorless and preamplifierless reception. Next, a set of measurements on one of the center WDM channels is performed where the LO power, received signal power, distance, and number of channels presented to the CRx are swept to evaluate the performance limits of colorless reception. Results reveal that the LO beating with optical noise incoming with the signal is a dominant noise source regardless of received signal power. In the high received signal power regime ( $\sim 0$  dBm/channel), the self-beat noise from out-of-band (OOB) channels is an additional major noise source especially for small LO-to-signal power ratio, short reach and large number of OOB channels. For example, at a received signal power of 0 dBm/channel after 1600 km transmission, the SNR difference between the fully filtered and colorless scenarios, where 1 and 16 channels are passed to the CRx respectively, grows from 0.5 to 3.3 dB as the LO power changes from 12 to 0 dBm. For low received power ( $\sim -12$  dBm/channel), the effect of OOB channels becomes minor while the receiver shot and thermal noises become more significant. We identify the common mode rejection ratio (CMRR) and sensitivity as the two important CRx specifications that impact the performance at high and low received signal power regimes, respectively. Finally, an excellent match between experimental and analytical SNRs is proven after the derived SNR model is fitted to the experimental data in a least-squares sense. The model is then used to predict that the CRx can operate colorlessly for a fully populated WDM spectrum with 80 channels provided that the LO-to-signal power ratio is properly set.

©2014 Optical Society of America

**OCIS codes:** (060.1660) Coherent communications; (060.2330) Fiber optics communications; (250.5300) Photonic integrated circuits; (250.3140) Integrated optoelectronic circuits.

---

## References and links

1. S. J. Savory, "Digital coherent optical receivers: algorithms and subsystems," *IEEE J. Sel. Top. Quantum Electron.* **16**, 1164–1179 (2010).

2. J. Kahn, "Modulation and detection techniques for optical communication systems," in *Proceedings of Optical Amplifiers and Their Applications/Coherent Optical Technologies and Applications*, Technical Digest (CD) (Optical Society of America, 2006), paper CThC1.
3. K. Roberts, D. Beckett, D. Boertjes, J. Berthold, and C. Laperle, "100G and beyond with digital coherent signal processing," *IEEE Commun. Mag.* **48**(7), 62–69 (2010).
4. C. Laperle, "Advances in high-speed ADCs, DACs, and DSP for optical transceivers," in *Proceedings of OFC* (17–21 March 2013).
5. S. J. Savory, "Digital filters for coherent optical receivers," *Opt. Express* **16**(2), 804–817 (2008).
6. E. Ip and J. M. Kahn, "Fiber impairment compensation using coherent detection and digital signal processing," *J. Lightwave Technol.* **28**, 502–519 (2010).
7. K. Roberts, "100G and beyond," in *Proceedings of 17th Opto-Electronics and Communications Conference (OECC)* (2012), pp. 144–145.
8. R. Essiambre, R. Ryf, N. Fontaine, and S. Randel, "Breakthroughs in photonics 2012: Space-division multiplexing in multimode and multicore fibers for high-capacity optical communication," *IEEE Photonics J.* **5**(2), 0701307 (2013).
9. K. Roberts and C. Laperle, "Flexible transceivers," in *Proceedings of European Conference and Exhibition on Optical Communication*, OSA Technical Digest (Optical Society of America, 2012), paper We.3.A.3.
10. D. Plant, Q. Zhuge, M. Morsy-Osman, M. Chagnon, X. Xu, and M. Qiu, "Flexible transceivers using adaptive digital signal processing for single carrier and OFDM," in *Proceedings of Optical Fiber Communication Conference (OFC)* (17–21 March 2013).
11. Cisco white paper, "Cisco Visual Networking Index: Forecast and methodology, 2012–2017" (Cisco, 2013), [http://www.cisco.com/en/US/solutions/collateral/ns341/ns525/ns537/ns705/ns827/white\\_paper\\_c11-481360.pdf](http://www.cisco.com/en/US/solutions/collateral/ns341/ns525/ns537/ns705/ns827/white_paper_c11-481360.pdf).
12. Emcore product web page, "ITLA (Integrable Tunable Laser Assembly)," <http://www.emcore.com/fiber-optics/telecom-tunable-dwdm/itla-integrable-tunable-laser-assembly/>.
13. L. Kazovsky, "Multichannel coherent optical communications systems," *J. Lightwave Technol.* **5**, 1095–1102 (1987).
14. L. Nelson, S. Woodward, S. Foo, M. Moyer, D. Beckett, M. O'Sullivan, and P. Magill, "Detection of a single 40 Gb/s polarization-multiplexed QPSK channel with a real-time intradyne receiver in the presence of multiple coincident WDM channels," *J. Lightwave Technol.* **28**, 2933–2943 (2010).
15. C. Xie, P. J. Winzer, G. Raybon, A. H. Gnauck, B. Zhu, T. Geisler, and B. Edvold, "Colorless coherent receiver using 3x3 coupler hybrids and single-ended detection," *Opt. Express* **20**(2), 1164–1171 (2012).
16. B. Zhang, C. Malouin, and T. J. Schmidt, "Towards full band colorless reception with coherent balanced receivers," *Opt. Express* **20**(9), 10339–10352 (2012).
17. L. Nelson, X. Zhou, R. Isaac, Y. Lin, J. Chon, and W. Way, "Colorless reception of a single 100Gb/s channel from 80 coincident channels via an intradyne coherent receiver," in *Proceedings of IEEE Photonics Conference* (2012), paper TuE4.
18. C. Doerr, P. Winzer, Y. Chen, S. Chandrasekhar, M. Rasras, L. Chen, T. Liow, K. Ang, and G. Lo, "Monolithic polarization and phase diversity coherent receiver in silicon," *J. Lightwave Technol.* **28**, 520–525 (2010).
19. Y. Painchaud, M. Pelletier, M. Poulin, F. Pelletier, C. Latrasse, G. Robidoux, S. Savard, J. Gagné, V. Trudel, M. Picard, P. Poulin, P. Sirois, F. D'Amours, D. Asselin, S. Paquet, C. Paquet, M. Cyr, M. Guy, M. Morsy-Osman, Q. Zhuge, X. Xu, M. Chagnon, and D. Plant, "Ultra-compact coherent receiver based on hybrid integration on silicon," in *Proceedings OFC* (2013), paper OM2J.
20. A. Matiss, R. Ludwig, J. Fischer, L. Molle, C. Schubert, C. Leonhardt, H. Bach, R. Kunkel, and A. Umbach, "Novel integrated coherent receiver module for 100G serial transmission," in *Proc. OFC* (2010), paper PDPB3.
21. C. Doerr, L. Zhang, P. Winzer, N. Weimann, V. Houtsma, T. Hu, N. Sauer, L. Buhl, D. Neilson, S. Chandrasekhar, Y. Chen, "Monolithic InP dual-polarization and dual-quadrature coherent receiver," *IEEE Photonics Technol. Lett.* **23**, 694–696 (2011).
22. D. Liang and J. E. Bowers, "Photonic integration: Si or InP substrates?" *Electron. Lett.* **45**(12), 578–581 (2009).
23. C. R. Doerr, L. L. Buhl, Y. Baeyens, R. Aroca, S. Chandrasekhar, X. Liu, L. Chen, Y. K. Chen, "Packaged monolithic silicon 112-Gb/s coherent receiver," *IEEE Photonics Technol. Lett.* **23**, 762–764 (2011).
24. M. Morsy-Osman, M. Chagnon, X. Xu, Q. Zhuge, M. Poulin, Y. Painchaud, M. Pelletier, C. Paquet, D. V. Plant, "Colorless and preamplifierless reception using an integrated Si-photonic coherent receiver," *IEEE Photonics Technol. Lett.* **25**, 1027–1030 (2013).
25. A. Carena, V. Curri, G. Bosco, P. Poggiolini, and F. Forghieri, "Modeling of the impact of nonlinear propagation effects in uncompensated optical coherent transmission links," *J. Lightwave Technol.* **30**, 1524–1539 (2012).
26. P. Poggiolini, A. Carena, V. Curri, G. Bosco, F. Forghieri, "Analytical modeling of nonlinear propagation in uncompensated optical transmission links," *IEEE Photonics Technol. Lett.* **23**, 742–744 (2011).
27. P. Poggiolini, "The GN model of non-linear propagation in uncompensated coherent optical systems," *J. Lightwave Technol.* **30**, 3857–3879 (2012).
28. Y. Painchaud, M. Poulin, M. Morin, and M. Têtu, "Performance of balanced detection in a coherent receiver," *Opt. Express* **17**(5), 3659–3672 (2009).
29. M. Nazarathy, W. Sorin, D. Baney, and S. Newton, "Spectral analysis of optical mixing measurements," *J. Lightwave Technol.* **7**, 1083–1096 (1989).
30. Although both LO and signal fields are stationary in their CW form, a modulated signal field is non-stationary rendering the final photocurrent difference  $\Delta i$  non-stationary. Hence, we apply both ensemble and time averaging to obtain a single argument time-averaged ACF from which the PSD is obtained using the Wiener–Khinchine theorem.

31. Despite that we neglect the ON-ON, SIG-ON and LO-LO terms in the final SNR expression derived, we provide the final expressions of the PSDs of each of those three noise contributions in appendix A (see subsection 6.4) for completeness.
  32. P. Ciblat and M. Ghogho, "Blind NLLS carrier frequency-offset estimation for QAM, PSK, and PAM modulations: Performance at low SNR," *IEEE Trans. Commun.* **54**, 1725–1730 (2006).
  33. I. Fatadin, D. Ives, and S. J. Savory, "Blind equalization and carrier phase recovery in a 16-QAM optical coherent system," *J. Lightwave Technol.* **27**, 3042–3049 (2009).
  34. ITU-T Recommendation G.975.1 Appendix I.9 (2004).
  35. J. Proakis, *Digital Communications* (McGraw Hill, 2001), Chap. 5.
  36. Although the PAPR depends on the accumulated CD, polarization orientation and number of channels, we use a PAPR value of 10 dB which represents an average value evaluated from the different raw waveforms captured by the real-time scope at various distances, number of channels, etc.
  37. S. Haykin, *Adaptive Filter Theory* (Prentice Hall, 1996), Chap. 11.
  38. Although assuming the same pulse shape, CD and polarization orientation is not true in practice, the discussion in appendix B regarding the scaling factor  $\beta$  will show that after a short transmission distance, the PSDs of the intensities of various WDM channels (and hence the power of the SIG-SIG beating) should eventually be the same regardless of the pulse shape, polarization orientation and CD.
- 

## 1. Introduction

The incessantly growing capacity demand in optical transport has been spurring extensive research efforts in the realm of coherent optical technology [1–10]. One key enabling component of this technology is the coherent optical receiver (CRx) that linearly maps the in-phase (I) and quadrature (Q) components of the received light in both orthogonal polarizations into the electrical domain by beating the received field with that of a local oscillator (LO) laser [1]. In addition, a CRx offers higher sensitivity compared to direct-detection [2] and enables the exploitation of  $M$ -ary quadrature amplitude modulation ( $M$ -QAM) formats consequently providing the needed larger spectral efficiency [2,3]. When incorporated with high speed analog-to-digital converters (ADCs), it also enables mitigating transmission impairments as well as compensating for hardware imperfections using digital signal processing (DSP) [1,5,6].

By incorporating coherent technology along with frequency division multiplexing (FDM) on multiple optical carriers, up to 400G coherent transceivers have been recently commercialized [7]. However, it still remains a challenge to meet the relentless growing network traffic demand [11]. Technological solutions such as space division multiplexing (SDM) that utilizes multiple fiber modes / cores have the potential to multiply the capacity per fiber [8]. Although being heavily investigated throughout the research community, SDM requires a potential replacement of the field installed fiber and developing novel enabling components. This may hinder near future field deployments of SDM. Another promising technological solution that is probably more suited for the near future is the concept of an agile/flexible software-defined optical network [9,10]. In the envisioned agile network, flexible coherent transceivers, that are capable of adapting to dynamic traffic needs and thus maximizing the network capacity, are key elements that need to be deployed at ingress/egress nodes. These flexible transceivers need to be smart, data-rate and modulation format agile and impairment aware/tolerant. In addition, the notion of agility necessitates the ability of the transceiver to transmit / receive at any optical frequency in order to adapt to the dynamic nature of the network. Since external cavity lasers (ECLs) fully tunable over the C or L band are commercially available [12], they can be incorporated as transmitter and LO lasers and hence, in principle, enable the transceiver to operate at any wavelength. At the transmitter side, tuning the laser simply varies the transmission wavelength without any observable change in the transmitted signal quality provided that the electro-optics performs similarly across the tuning range. However on the receiver side, the situation is more complex. A CRx can in principle operate in a colorless fashion by utilizing the LO laser for channel selection. Such a scheme mandates removing the DEMUX filter before the receiver which is beneficial on one hand as it reduces cost and footprint besides offering the desired transceiver flexibility, but on the other hand, it may degrade the performance depending on various parameters e.g., the number of channels co-incident at the receiver with the channel of interest, the LO power, etc. Colorless reception in the context of coherent optical

communication was studied from a theoretical standpoint more than two decades ago [13]; however, the absence of commercial narrow linewidth lasers and high speed integrated circuits (ICs) prevented any practical implementation. Recently, there have been some reports on experimental colorless coherent reception by utilizing either a conventional CRx front-end followed by single-ended detection [14], which suffers from limited maximum channel count and poor dynamic range due to the inability to reject the self-beat common mode noise, or a more complicated receiver front-end followed by single-ended detection to enable rejecting the self-beat noise [15]. Later in [16], Zhang et al. presented design guidelines and performance limits of colorless reception employing balanced detection based on simulation and analytical predictions. More recently in [17], the authors demonstrated experimentally the use of an integrated PLC-based balanced coherent receiver for colorless reception of one 100G channel among 80 WDM channels.

The recent tremendous progress of the photonic integration technology allows for cost effective and volume production of coherent receivers employing balanced photodetectors which are more suited for colorless operation. Recently, integrated dual-polarization phase-diversity balanced coherent receiver photonic integrated circuits (PICs) have been demonstrated in both Si [18,19] and InP [20,21]. Si has advantages over InP as a host material since it can be made into larger wafers allowing for lower cost chips [22]. In addition, the world of analog ICs now offers linear and differential transimpedance amplifiers (TIAs) with variable gain control and bandwidths commensurate with the baud rates at which a coherent transceiver operates. Recently, researchers reported TIAs packaged and wire bonded to the PIC in one module [19,20,23]. The TIAs enhance the receiver dynamic range and provide the target voltage swing required by the analog-to-digital converters (ADCs). In addition, TIAs accompanied with the high sensitivity of coherent reception potentially enable preamplifierless operation in which the optical preamplifier prior to the receiver is removed and essentially replaced by the electrical TIAs thus saving footprint and power consumption. Recently in our work in [24], we evaluated the sensitivity limits of the Si-photonic integrated balanced CRx presented in [19] when employed in colorless and preamplifierless reception of single channel 112 Gbps PDM-QPSK and 224 Gbps PDM-16QAM. Also, we have shown preliminary results of colorless reception of  $16 \times 112$  Gbps PDM-QPSK WDM channels.

In this paper, we extend our work in [24] and study from theoretical and experimental standpoints the performance limits of the Si-photonic CRx when employed in a WDM colorless configuration. Firstly, we show the building blocks and introduce the key characterization results of the CRx assembly. Secondly, we develop rigorously an analytical expression of the SNR at the CRx output in the case of colorless reception taking into consideration all sources of noise namely, LO-ON, SIG-SIG, SIG-ON, ON-ON and LO-LO beatings as well as the receiver shot and thermal noises, where SIG stands for signal and ON stands for optical noise incoming with the signal. As will be later explained in details, the ON incoming with the signal contains contributions of both the amplified spontaneous emission (ASE) noise from in-line optical amplifiers and the fiber nonlinearity (NL) induced noise, which can be both modeled, according to [25–27], as additive white Gaussian noise (AWGN) in the context of dispersion unmanaged transmission (UT). Compared to [16] where an analytical SNR expression was also given, the derivation performed in this manuscript, which is based on evaluating the autocorrelation functions and the power spectral densities of all terms in the differential photocurrent, is more rigorous. In addition, we propose an analytical expression for an effective common mode rejection ratio (CMRR) for the SIG-SIG beating term which takes into account the frequency dependent nature of the power imbalance and the skew mismatch between the  $P$  and  $N$  photodiodes of the CRx weighted by the power spectral density of the received signal intensity. This parameter was only arbitrarily defined in [16]. Furthermore, another distinguishing difference from the model in [16] is the inclusion of the impact of fiber nonlinearity as excess AWGN in addition to the conventional ASE noise from in-line EDFAs. Thirdly, we study experimentally the performance of the CRx in a fully colorless and preamplifierless reception of  $16 \times 112$  Gbps PDM-QPSK WDM channels. Using a maximum LO power of 15.5 dBm, we evaluate the BER of each channel at various

transmission distances at received signal powers of  $-3$  and  $-21$  dBm per channel. Next, we restrict our measurements to one of the center channels of the WDM spectrum and perform an extensive set of measurements where we sweep the LO power, the received signal power, the distance and the number of channels presented to the CRx. This set of measurements aims at evaluating the performance limits of the CRx when used for colorless reception. All trends observed in the experimental results match those expected from simulations in [16]. In fact, results reveal that in the regime of high received signal power, the residual SIG-SIG beat noise from the out-of-band (OOB) channels degrades the performance especially for lower LO to signal power ratios and this degradation becomes relatively less pronounced as the transmission distance increases. In the regime of low received signal power, the shot noise and receiver thermal noise degrade the performance especially for very low LO powers and short transmission distances. Two key CRx specifications that dictate the achievable dynamic operating range are highlighted namely the responsivity and the CMRR, which impact the performance in the regimes of low and high received signal powers, respectively. Finally, we employ our experimental SNR results to fit the proposed analytical model to our experimental data using the least-squares criterion. An excellent match between experimental and analytical SNRs is found. We finally use the model to extrapolate the SNR curves beyond our experimental capabilities and predict the SNR when the number of channels is larger than 16. We conclude that the CRx allows for colorless selection of the test channel out of a fully populated WDM spectrum with 80 channels while achieving error-free operation after 4800 km transmission provided that the LO and received signal powers are properly set.

This paper is organized as follows. In section 2, the architecture of the SiP CRx assembly is presented and the main device-level characterization results are introduced. Section 3, supported by derivations in appendices A and B and the list of mathematical symbols used in Table 1, presents an analytical model for the SNR at the output of the CRx where various noise sources that impact the SNR in a colorless reception scheme are outlined. In section 4, we depict the system-level WDM experimental results obtained using the CRx on  $16 \times 112$  Gbps PDM-QPSK channels where the impact of LO power, received signal power, number of channels and transmission distance on the performance of colorless reception are studied experimentally and compared to theory presented in section 3. Finally, concluding remarks are given in section 5.

## 2. Si-photonic integrated balanced coherent receiver design and characterization

The coherent receiver is based on silicon photonics (SiP) technology which enables a very compact design. Figure 1(a) gives a view of the assembly. Strip waveguides of 220 nm (height)  $\times$  500 nm (width) are used to convey the light in the optical chip. A single-mode and a PM fiber whose end facets are polished at an angle close to  $45^\circ$  are used to couple the light from the data-carrying signal and LO respectively into the SiP chip. Polarization diversity is obtained via a 2D surface grating that couples orthogonal linear polarization states from the data-carrying signal in two separate waveguides. For the LO, a 1D grating coupler is used, followed by a  $1 \times 2$  multimode interference (MMI) splitter. The light from each polarization of the incoming signal is combined to the light from the split LO using  $2 \times 4$  MMI couplers. The light from the two  $2 \times 4$  MMI couplers is coupled out of the chip using eight 1D grating coupler and sent to two  $1 \times 4$  photodiode arrays which are flip chip mounted onto the  $6 \text{ mm} \times 6 \text{ mm}$  SiP chip. The photodiodes are used in balanced pairs and connected to TIAs. The SiP chip and TIAs are fixed onto a ceramic substrate. RF lines connect the AC-coupled differential outputs of the TIAs to eight pins on the CRx package in a GSGSG configuration. For the sake of the present experiments, an RF interface board is used to provide access to a set of four single-ended outputs ( $XI^+$ ,  $XQ^+$ ,  $YI^+$  and  $YQ^+$ ) on K connectors. The assembled CRx presents a small-signal bandwidth of 22 GHz and a quadrature error of less than  $3^\circ$ . The effective responsivity at 192.9 THz averaged over all 8 photodiodes (PDs) is 0.025 and 0.029 A/W for the SIG and LO ports, respectively. These effective responsivities include (besides the PD responsivities) the 3 dB intrinsic loss of the polarization beam splitter (PBS) and the 6 dB intrinsic loss of the  $2 \times 4$  MMI coupler in addition to their excess loss as well as

coupling losses in and out of the SiP chip. Figure 1(b) shows the overall small signal frequency response including the photodiodes, the TIA and the RF lines on the ceramic. The overshoot in the response is due to the TIA. Finally, Figs. 2(a) and 2(b) show the CMRR versus frequency curves for the LO and SIG ports, respectively measured at the four output ports at 192.9 THz according to the procedure described in [28]. We notice that the CRx provides a DC CMRR better than  $-14$  and  $-18$  dB for the LO and SIG ports, respectively.

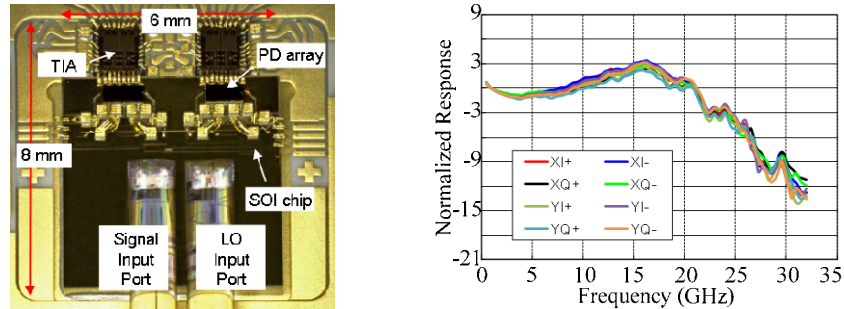


Fig. 1. (a) Picture of the PIC of the CRx showing the main building blocks, (b) Overall frequency response of the Si-phonic CRx assembly.

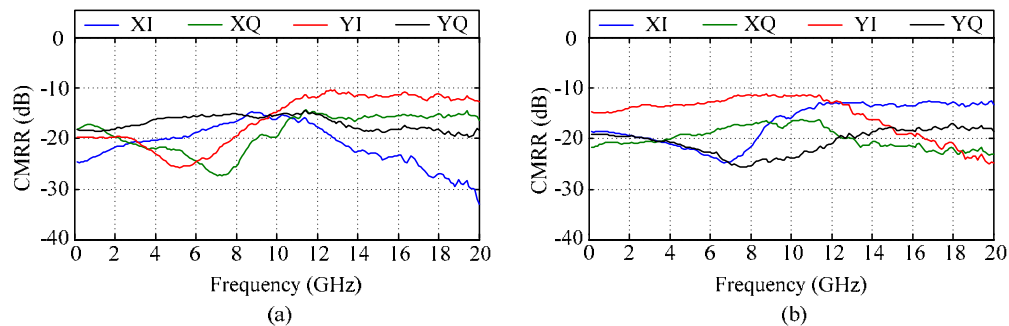


Fig. 2. CMRR versus frequency curves measured at 192.9 THz at the four output RF ports of the CRx when light is applied at the (a) signal port, (b) LO port.

### 3. Theoretical performance evaluation of a colorless coherent receiver

After laying out the CRx chip architecture, the performance of the CRx when employed for colorless coherent reception is evaluated analytically in this section. We present the various noise sources that dictate the performance of colorless CRx operation, highlighting the key CRx specifications that impact the performance. An analytical expression for the SNR at the CRx output is developed. The SNR analytical model derived will be employed later in the manuscript to verify the experimental results presented in forthcoming sections.

Although an analytical SNR expression for the colorless scenario when employing coherent balanced detection has been presented in [16], a more rigorous and complete approach is adopted in this manuscript. Without loss of generality, we consider one of the four CRx output ports  $\{XI, XQ, YI, YQ\}$  and derive an expression of the autocorrelation function (ACF) (and then the power spectral density PSD) of the differential photocurrent after imperfect balanced detection. The desired signal term as well as various noise terms in the final differential photocurrent are identified and their respective ACFs (and PSDs) are derived methodically in terms of input fields to the CRx. Compared to [16], the expressions we obtain hereafter are more complete and the systematic approach adopted throughout the derivation leads to an expression for an “effective CMRR” which is a system parameter that quantifies the ability of balanced detection to reject the SIG-SIG beating, taking into account the frequency dependent nature of the power imbalance and the skew mismatch between the  $P$  and  $N$  photodiodes of the CRx weighted by the PSD of the received signal intensity. This quantity termed “effective CMRR” was proposed and only arbitrarily defined in [16].

Furthermore, another distinguishing difference from the work in [16] is that the optical noise incoming with the received signal assumed in our model contains the impact of not only the ASE noise from in-line EDFAs but also the induced noise due to fiber nonlinearity where both noise sources can be modeled as AWGN in the context of dispersion unmanaged transmission [25–27].

The procedure used to derive the ACFs and PSDs for various terms in the differential photocurrent follows the one outlined in [29]. We start by writing the photocurrents at the outputs of the  $P$  and  $N$  photodiodes (PDs), denoted by  $i^P(t)$  and  $i^N(t)$ , in terms of the real electric fields of the signal (all WDM channels and their accompanying optical noise) and LO as

$$\begin{aligned} i^P(t) &= \left[ \sum_{i=1}^{N_{ch}} \sqrt{R_{SIG,i}^P} (E_{SIG,i}(t) + E_{ON,i}(t)) + \sqrt{R_{LO,s}^P} (E_{LO}(t)) \right]^2 + i_{sh}^P + i_{th}^P \\ &\approx 2\sqrt{R_{SIG,s}^P R_{LO,s}^P} [E_{SIG,s}(t)E_{LO}(t) + E_{ON,s}(t)E_{LO}(t)] \\ &\quad + \sum_{i=1}^{N_{ch}} R_{SIG,i}^P [E_{SIG,i}^2(t) + E_{ON,i}^2(t) + 2E_{SIG,i}(t)E_{ON,i}(t)] + R_{LO,s}^P E_{LO}^2(t) + i_{sh}^P + i_{th}^P, \end{aligned} \quad (1)$$

$$\begin{aligned} i^N(t) &= \left[ \sum_{i=1}^{N_{ch}} \sqrt{R_{SIG,i}^N} (E_{SIG,i}(t-\delta) + E_{ON,i}(t-\delta)) - \sqrt{R_{LO,s}^N} (E_{LO}(t-\delta)) \right]^2 + i_{sh}^N + i_{th}^N \\ &\approx -2\sqrt{R_{SIG,s}^N R_{LO,s}^N} [E_{SIG,s}(t-\delta)E_{LO}(t-\delta) + E_{ON,s}(t-\delta)E_{LO}(t-\delta)] \\ &\quad + \sum_{i=1}^{N_{ch}} R_{SIG,i}^N [E_{SIG,i}^2(t-\delta) + E_{ON,i}^2(t-\delta) + 2E_{SIG,i}(t-\delta)E_{ON,i}(t-\delta)] + R_{LO,s}^N E_{LO}^2(t-\delta) + i_{sh}^N + i_{th}^N, \end{aligned} \quad (2)$$

where  $E_{SIG,i}$ ,  $E_{ON,i}$ ,  $E_{LO}$  are the real-valued electric fields of the  $i^{\text{th}}$  signal out of  $N_{ch}$  WDM signals presented to the CRx in colorless scheme, optical noise accompanying the  $i^{\text{th}}$  WDM signal, and local oscillator (LO) all measured at the input to the CRx, respectively. Without loss of generality, we assume that channel  $s \in \{1, 2, \dots, N_{ch}\}$  is the desired channel in the WDM spectrum. Also, we assume that the LO frequency is tuned such that the frequency offset between the LO and the center frequency of channel  $s$  is much less than its baseband bandwidth, i.e. intradyne reception is used. Thus, the LO beating with OOB channels will lie outside the CRx bandwidth and hence was eliminated in the second equality of Eqs. (1) and (2). Also, we assume that  $E_{ON,i}$  is the total incoming optical noise with the  $i^{\text{th}}$  WDM channel which contains both the ASE noise from in-line optical amplifiers and the noise induced due to fiber NL. According to [25–27], the NL-induced noise in case of dispersion uncompensated transmission can be modeled accurately as AWGN similar to ASE noise and hence, both additive noises can be combined in one total optical noise field which finally results in a worse optical signal-to-noise ratio (OSNR) governing the system performance [27]. According to [27], this modified OSNR at the CRx input is defined as  $OSNR = P_{SIG}/P_{ON}$  where  $P_{ON} = P_{ASE} + P_{NL}$  is the total optical noise power due to both ASE and NL contributions. As will be shown in subsection 4.2.3, both the ASE noise and the NL-induced noise scale linearly with transmission distance (assuming the NL-induced noise contributions from multiple spans are approximately summed incoherently [25,27]) and will be indistinguishable in our experimental data since the launch power was kept constant throughout the measured data. In addition,  $R_{SIG,i}^P, R_{SIG,i}^N$  are the effective responsivities at the wavelength of the  $i^{\text{th}}$  channel measured at the  $P$  and  $N$  PDs to the optical power applied to the signal port. In addition,  $R_{LO,s}^P, R_{LO,s}^N$  are the effective responsivities measured at the  $P$  and  $N$  PDs to the LO power applied at the wavelength of channel  $s$ . It is also noteworthy that the effective responsivities defined above take into account (besides the photodiode responsivities) the 3 dB intrinsic loss of the polarization beam splitter (PBS) and the 6 dB

intrinsic loss of the  $2 \times 4$  MMI coupler in addition to their excess loss as well as coupling losses in and out of the SiP chip. In addition,  $\delta$  is the time skew between the  $P$  and  $N$  paths measured from the output of the MMI couplers up to current subtraction which occurs inside the TIA. Finally,  $i_{sh}^P, i_{sh}^N$  are the shot noise currents at the  $P$  and  $N$  photodiode outputs and  $i_{th}^P, i_{th}^N$  are the input-referred thermal noise currents at the  $P$  and  $N$  inputs of the TIA, respectively. In Eqs. (1) and (2), we also neglect the SIG-SIG beating between each WDM channel with its neighbors and consider only the beating between each signal with itself which lies within the CRx bandwidth. Although a portion of the spectral components from the beating between two adjacent WDM channels may fall inside the baseband CRx bandwidth, this portion is negligible compared to the SIG-SIG beating of each channel with itself especially after being lowpass filtered by the CRx frequency response.

Similar to [29], we express the real-valued fields in Eqs. (1) and (2) in terms of baseband complex envelopes (denoted by boldface symbols throughout the manuscript) as

$$\begin{aligned} E_{SIG,i}(t) &= \text{Re}\left\{\tilde{E}_{SIG,i}(t)e^{j2\pi\nu_{SIG,i}t}\right\}, \\ E_{LO}(t) &= \text{Re}\left\{\tilde{E}_{LO}(t)e^{j2\pi\nu_{LO}t}\right\}, \\ E_{ON,i}(t) &= \text{Re}\left\{\tilde{E}_{ON,i}(t)e^{j2\pi\nu_{SIG,i}t}\right\}, \end{aligned} \quad (3)$$

where  $\tilde{E}_k(t)$  is the baseband complex envelope representing the real bandpass field  $E_k(t)$  and  $e^{j2\pi\nu_k t}$  is the complex-valued carrier at the optical frequency  $\nu_k$ . Now, one can use the relation

$$\begin{aligned} E_1(t)E_2(t) &= \text{Re}\left\{\tilde{E}_1(t)e^{j2\pi\nu_1 t}\right\} \cdot \text{Re}\left\{\tilde{E}_2(t)e^{j2\pi\nu_2 t}\right\} \\ &= \frac{1}{2}\text{Re}\left\{\tilde{E}_1(t)\tilde{E}_2^*(t)e^{j2\pi(\nu_1-\nu_2)t}\right\} + \frac{1}{2}\text{Re}\left\{\tilde{E}_1(t)\tilde{E}_2(t)e^{j2\pi(\nu_1+\nu_2)t}\right\}, \end{aligned} \quad (4)$$

to re-write Eqs. (1) and (2) noting that the terms at the sum of optical frequencies will be filtered out, yielding

$$\begin{aligned} i^P(t) &= 2\sqrt{R_{SIG,s}^P R_{LO,s}^P} \cdot \frac{1}{2}\text{Re}\left\{\tilde{E}_{SIG,s}(t)\tilde{E}_{LO}^*(t)e^{j2\pi\Delta\nu t} + \tilde{E}_{ON,s}(t)\tilde{E}_{LO}^*(t)e^{j2\pi\Delta\nu t}\right\} \\ &\quad + \frac{1}{2}\sum_{i=1}^{N_{ch}} R_{SIG,i}^P \left[ \left| \tilde{E}_{SIG,i}(t) \right|^2 + \left| \tilde{E}_{ON,i}(t) \right|^2 + 2\text{Re}\left\{\tilde{E}_{SIG,i}(t)\tilde{E}_{ON,i}^*(t)\right\} \right] + R_{LO,s}^P \cdot \frac{1}{2}\left| \tilde{E}_{LO}(t) \right|^2 + i_{sh}^P + i_{th}^P, \end{aligned} \quad (5)$$

$$\begin{aligned} i^N(t) &= -2\sqrt{R_{SIG,s}^N R_{LO,s}^N} \cdot \frac{1}{2}\text{Re}\left\{\tilde{E}_{SIG,s}(t-\delta)\tilde{E}_{LO}^*(t-\delta)e^{j2\pi\Delta\nu(t-\delta)} + \tilde{E}_{ON,s}(t-\delta)\tilde{E}_{LO}^*(t-\delta)e^{j2\pi\Delta\nu(t-\delta)}\right\} \\ &\quad + \frac{1}{2}\sum_{i=1}^{N_{ch}} R_{SIG,i}^N \left[ \left| \tilde{E}_{SIG,i}(t-\delta) \right|^2 + \left| \tilde{E}_{ON,i}(t-\delta) \right|^2 + 2\text{Re}\left\{\tilde{E}_{SIG,i}(t-\delta)\tilde{E}_{ON,i}^*(t-\delta)\right\} \right] \\ &\quad + R_{LO,s}^N \cdot \frac{1}{2}\left| \tilde{E}_{LO}(t-\delta) \right|^2 + i_{sh}^N + i_{th}^N, \end{aligned} \quad (6)$$

where  $\Delta\nu = \nu_{SIG,s} - \nu_{LO}$  is the frequency offset between the center frequency of channel  $s$  and the LO. Next, the difference between the  $P$  and  $N$  photocurrents in Eqs. (5) and (6), which represents the final differential photocurrent, can be written as

$$\begin{aligned} \Delta i(t) &= i^P(t) \otimes h^P(t) - i^N(t) \otimes h^N(t) \\ &= \Delta i_{LO-SIG}(t) + \Delta i_{LO-ON}(t) + \Delta i_{SIG-SIG}(t) + \Delta i_{ON-ON}(t) + \Delta i_{SIG-ON}(t) + \Delta i_{LO-LO}(t) + \Delta i_{sh}(t) + \Delta i_{th}(t), \end{aligned} \quad (7)$$



where  $\otimes$  denotes convolution,  $h^P(t)$  and  $h^N(t)$  are the impulse responses of the  $P$  and  $N$  paths from the PD outputs up to current subtraction in the TIAs, i.e. they include the impact of limited bandwidth of PDs, TIA and wire bonding between them. Ideally,  $h^P(t)$  and  $h^N(t)$  should be the same but the slight difference between the frequency responses should be taken into account since it will impact the frequency dependence of the common mode rejection ratio of the CRx. In Eq. (7), we separate the individual contributions in the final photocurrent where the first term is the LO-SIG beating term which is the desired signal term resulting from subtracting the first terms of Eqs. (5) and (6) after convolving each of them with  $h^P(t)$  and  $h^N(t)$ . The next terms in Eq. (7) represent all noise contributions in the final differential photocurrent due to LO-ON, SIG-SIG, ON-ON, SIG-ON, LO-LO beatings as well as shot and thermal noises which also result from subtracting all terms subsequent to the LO-SIG term in Eqs. (5) and (6) after convolving with the  $P$  and  $N$  impulse responses.

In case of ideal balanced detection, i.e.  $R_{SIG,i}^P = R_{SIG,i}^N$ ,  $R_{LO,s}^P = R_{LO,s}^N$ ,  $h^P(t) = h^N(t)$  and  $\delta = 0$ , the SIG-SIG, ON-ON, SIG-ON and LO-LO noise terms in Eq. (7) cancel out since these terms are common to both the  $P$  and  $N$  PDs and will be entirely rejected. In this case, the LO-ON beating as well as the thermal and shot noises become the only noise sources contributing to the final differential photocurrent. However in reality, imperfect balanced detection due to frequency dependent power imbalance and skew mismatch between the  $P$  and  $N$  photocurrents will lead to residual noise power due to imperfect common mode rejection. For the rest of the derivation, we assume imperfect balanced detection and derive the time-averaged ACF of  $\Delta i(t)$  in Eq. (7), which is denoted by  $\bar{\Gamma}_{\Delta i}(\tau)$ , as follows

$$\bar{\Gamma}_{\Delta i}(\tau) = \overline{\langle \Delta i(t) \Delta i(t-\tau) \rangle} \\ = \bar{\Gamma}_{\Delta i_{LO-SIG}}(\tau) + \bar{\Gamma}_{\Delta i_{LO-ON}}(\tau) + \bar{\Gamma}_{\Delta i_{SIG-SIG}}(\tau) + \bar{\Gamma}_{\Delta i_{ON-ON}}(\tau) + \bar{\Gamma}_{\Delta i_{SIG-ON}}(\tau) + \bar{\Gamma}_{\Delta i_{LO-LO}}(\tau) + \bar{\Gamma}_{\Delta i_{sh}}(\tau) + \bar{\Gamma}_{\Delta i_{th}}(\tau), \quad (8)$$

where  $\langle \rangle$  denotes ensemble (statistical) averaging and the bar denotes time averaging. In deriving Eq. (8), all the cross correlation terms between currents from various sources can be shown to cancel out by the use of statistical independence between different fields as well as the fact that  $\langle \tilde{E}(t) \rangle = 0$  for all fields. This finally means that the ACF of the final photocurrent is the sum of the ACFs of all individual terms in Eq. (7). The next step is to find the individual ACFs, i.e. each term in Eq. (8), in terms of the input fields as well as the CRx parameters. After that, we make use of the Wiener-Khintchine theorem for non-stationary signals [30] which states that the power spectral density (PSD) of a non-stationary signal is the Fourier transform (FT) of its time-averaged ACF  $\bar{\Gamma}_E(\tau)$  which can be applied to Eq. (8), yielding

$$S_{\Delta i}(f) = \text{FT} \{ \bar{\Gamma}_{\Delta i}(\tau) \} \\ = S_{\Delta i_{LO-SIG}}(f) + S_{\Delta i_{LO-ON}}(f) + S_{\Delta i_{SIG-SIG}}(f) + S_{\Delta i_{ON-ON}}(f) + S_{\Delta i_{SIG-ON}}(f) + S_{\Delta i_{LO-LO}}(f) + S_{\Delta i_{sh}}(f) + S_{\Delta i_{th}}(f) \quad (9) \\ \approx S_{\Delta i_{LO-SIG}}(f) + S_{\Delta i_{LO-ON}}(f) + S_{\Delta i_{SIG-SIG}}(f) + S_{\Delta i_{sh}}(f) + S_{\Delta i_{th}}(f),$$

where in the last equality, we neglect the ON-ON, SIG-ON and LO-LO contributions to the overall photocurrent difference [31]. The argument behind neglecting those three terms is that they were found to be experimentally negligible compared to the SIG-SIG beating. In fact, this experimental observation is intuitive since the SIG-SIG, ON-ON and SIG-ON beatings are proportional to  $P_{SIG}^2$ ,  $P_{ON}^2$  and  $P_{SIG}P_{ON}$ , respectively, where  $P_{SIG}, P_{ON}$  are the average optical powers of the received signal and the total optical noise real-valued fields within the bandwidth of one channel. Given that the OSNR level (defined similar to [27] as the ratio between the optical signal power to the total optical noise power including both ASE and NL-

induced noises) at the CRx input at which error-free operation is achieved is relatively high (e.g.  $> 12$  dB in 0.1 nm for 28 Gbaud PDM-QPSK), we can notice that ON-ON and SIG-ON beatings are negligible compared to SIG-SIG beating. Regarding the LO-LO beating,  $S_{\Delta i_{LO-LO}}(f)$  is proportional to  $P_{LO}^2 RIN(f)$ , where  $P_{LO}$  is the average optical power of the LO field and  $RIN(f)$  is the PSD of the relative intensity noise of the LO laser. Since the LO used in experiments had a  $RIN$  of around  $-145$  dB/Hz and the maximum LO power used throughout experiments is 15.5 dBm, the LO RIN contribution to the final photocurrent was experimentally found to be negligible.

$$SNR = \frac{\int_{-\infty}^{\infty} S_{\Delta f_{LO-SIG}}(f) |H_{rx-DSP}(f)|^2 df}{\int_{-\infty}^{\infty} [S_{\Delta f_{LO-ON}}(f) + S_{\Delta f_{SIG-SIG}}(f) + S_{\Delta f_{hh}}(f) + S_{\Delta f_{lh}}(f)]^{AC} |H_{rx-DSP}(f)|^2 df} = \frac{P_{\Delta f_{LO-SIG}}}{\sigma_{\Delta f_{LO-ON}}^2 + \sigma_{\Delta f_{SIG-SIG}}^2 + \sigma_{\Delta f_{hh}}^2 + \sigma_{\Delta f_{lh}}^2}, \quad (10)$$

$$SNR = \frac{2P_{LO}P_{SIG}}{2c_1P_{LO}P_{ON} + c_2(\sigma_{\Delta f_{ch}}^2 + \sigma_{\Delta f_{th}}^2) + \overline{CMRR}_{SIG}N_{ch}BP_{SIG}^2}, \quad (11)$$

$$CMRR_{SIG} = \frac{\int_{-\infty}^{\infty} \left| H^P(f) R_{SIG}^P - H^N(f) e^{j2\pi f \delta} \sqrt{R_{SIG}^N R_{LO}^N} \right|^2 \left[ \tilde{S}_{\tilde{SIG}}^{AC}(f) \right] \left| H_{rx-DSP}(f) \right|^2 df}{\int_{-\infty}^{\infty} \left| H^P(f) \sqrt{R_{SIG}^P R_{LO}^P} + H^N(f) e^{j2\pi f \delta} \sqrt{R_{SIG}^N R_{LO}^N} \right|^2 \left| G(f) \right|^2 \left| H_{rx-DSP}(f) \right|^2 df} \quad (10)$$

Also, the scaling factor  $\beta$  is defined in appendix A as the ratio between the AC power from the filtered photocurrent generated by the field intensity of one channel and its DC

electrical power. In appendix B, a more thorough study of  $\beta$  is performed to assess its dependence on the residual chromatic dispersion (CD) and polarization orientation of the received signal. It should be noted that Eq. (11) was proved by considering only one of the four outputs provided by the CRx; however, the derived SNR expression has the same form for all ports except for using the parameters of each port, e.g. responsivities and frequency responses. Hence, an overall average SNR can be calculated by averaging the SNRs calculated at the four ports.

The quantity  $\overline{CMRR}_{SIG}$  denotes the so-called “effective CMRR” of the SIG-SIG beating which is a system parameter (not a CRx parameter) that quantifies the ability of imperfect balanced detection to reject the common-mode SIG-SIG beating while taking into account the CRx parameters, namely, the effective responsivities, frequency responses and time skew for the  $P$  and  $N$  paths up to current subtraction inside the TIAs, as well as the system parameters, namely, the residual CD, polarization orientation and pulse shape which are imbedded in the PSD of the intensity  $S_{|\tilde{E}_{SIG}|^2}^{AC}(f)$  (see Eq. (40) in appendix A). In fact, the effective CMRR

definition given above contains the quantity  $\left| H^P(f)R_{SIG}^P - H^N(f)e^{j2\pi f\delta}R_{SIG}^N \right|^2$  which quantifies the CRx ability to reject the common mode SIG-SIG beating incoming from the SIG port. Since this rejection ability is frequency dependent, the effective CMRR expression also weighs this quantity using the PSD of the common mode quantity being rejected, i.e. the field intensity, as represented by  $S_{|\tilde{E}_{SIG}|^2}^{AC}(f)$  in the  $\overline{CMRR}_{SIG}$  expression. Dividing by the

denominator in the effective CMRR expression means that  $\overline{CMRR}_{SIG}$  is a measure of how strong the power of the residual common mode SIG-SIG beating is compared to that of the differential LO-SIG beating. This explains why the denominator is proportional to the product of responsivities of the SIG and LO ports whereas the numerator is proportional to the square of the responsivity of the SIG port. Finally, we should note that the above expression for the effective CMRR was obtained in a systematic and rigorous manner in the derivation included in appendix A. This differs from [16] where the authors proposed the interesting concept of an effective CMRR, being a single averaged value applied to the common mode beating and defined quite arbitrarily as the CMRR value at half the Nyquist frequency.

#### 4. WDM experiment, results and discussion

In this section, we evaluate experimentally the system-level performance of the SiP CRx module whose chip architecture was described in section 2. First, we introduce the experimental setup used to assess the CRx performance using  $16 \times 112$  Gbps PDM-QPSK WDM channels. Subsequently, we present the experimental results, starting with the BER for all 16 channels at different distances and received signal powers. Afterwards, we present a series of extensive measurements obtained for one of the center WDM channels where the LO power, received signal power, distance, and number of channels presented to the CRx are swept. A thorough discussion of the results is given, focusing on the major noise sources affecting the performance of the colorless operation of the CRx for different operating parameters in view of the analytical SNR expression derived in section 3. Finally, we use the experimental SNR data to fit the analytical SNR expression derived in section 3. The fitted SNR model is then used to predict the SNR at other operating parameters beyond our experimental capabilities, e.g. larger number of WDM channels.

##### 4.1. Experimental setup

Figure 3 shows the experimental setup used in various WDM measurements presented in the following subsections. CW light from 16 distributed feedback (DFB) lasers (50 GHz spaced and centered at 192.9 THz) are multiplexed using a 50 GHz arrayed waveguide grating WDM multiplexer and then bulk modulated by means of a QAM transmitter. The QAM transmitter comprises a single polarization LiNbO<sub>3</sub> double-nested Mach-Zehnder modulator and two

high-speed RF amplifiers to drive the two quadratures. Binary I and Q electrical signals are fed to the QAM transmitter from two MICRAM DACs driven by two Xilinx FPGAs at 28 Gbaud to realize  $16 \times 112$  Gbps PDM-QPSK WDM channels on a 50 GHz grid. Then, a polarization beam splitter (PBS), variable optical delay line (VODL) and polarization beam combiner (PBC) are employed for PDM emulation with a decorrelation delay between the two orthogonal polarizations equivalent to 700 symbols at 28 Gbaud. After optical amplification, odd and even WDM channels are decorrelated by  $\sim 7.5$  ns using a 50 GHz interleaver / de-interleaver. The resulting optical signal was attenuated using a variable optical attenuator (VOA) to set the launch power at  $-2$  dBm per channel which was experimentally found to be the optimum launch power that achieves the right balance between fiber nonlinearity and ASE noise from in-line EDFAs. At this launch power, which was kept constant throughout the experiment, both ASE and NL-induced noises are non-negligible and hence, they were both included in the SNR model presented in section 3. Next, the resulting signal was launched into a recirculating loop containing four spans of 80 km of SMF-28e<sup>+</sup> fiber, each span being followed by an erbium-doped fiber amplifier (EDFA) having a noise figure of 5 dB. In addition, an optical WaveShaper from Finisar is inserted after the second in-line EDFA for gain flattening.

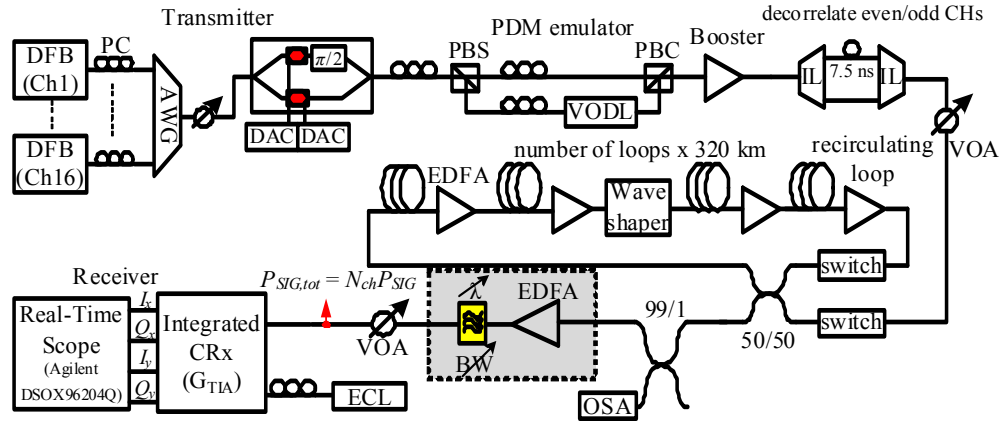


Fig. 3. Experimental setup for WDM experiments, (IL: Interleaver, DFB laser: Distributed Feedback laser, AWG: Arrayed Waveguide Grating, PBS: Polarization Beam Splitter, PBC: Polarization Beam Combiner, VODL: Variable Optical Delay Line, ECL: External Cavity Laser, OSA: Optical Spectrum Analyzer, VOA: Variable Optical Attenuator).

At the output of the loop, no noise loading is performed hence the OSNR is only dictated by the ASE noise from in-line EDFAs around the loop as well as the fiber NL-induced noise. We used a 99:1 coupler to monitor the WDM spectrum on an optical spectrum analyzer (OSA) and to measure the OSNR. After 1600, 3200 and 4800 km of transmission, i.e. 5, 10 and 15 loops respectively, the measured OSNRs, assuming a 0.1 nm reference bandwidth, were 21.4, 18.9 and 17.6 dB, respectively. After the 99:1 coupler, we distinguish between two reception configurations: 1) a fully colorless configuration in which the attenuated signal carrying all 16 channels is fed directly to the signal port of the CRx module at a total power level  $P_{SIG,tot} (= N_{ch}P_{SIG})$  controlled by the VOA, i.e. elements in the grey shaded box are skipped, 2) another configuration in which the WDM signal is first amplified to a constant total power of 22 dBm, subsequently filtered using a wavelength & bandwidth tunable filter, and then attenuated using a VOA to set the total received power level ( $P_{SIG,tot}$ ) before finally entering the CRx, i.e. elements in the grey shaded box are employed. Inserting the EDFA prior to the CRx allows us to sweep  $P_{SIG,tot}$ , and subsequently the received power per channel ( $P_{SIG}$ ), to levels larger than the received power from the loop. As will be observed in the next subsection, the sweep range of  $P_{SIG}$  extends up to 5 dBm per channel in order to evaluate the impact of colorless reception on the dynamic range of the CRx. After the EDFA, the wavelength & bandwidth tunable filter had its center frequency constantly set to that of

channel 9 (with channel 1 having the smallest frequency) and its bandwidth swept to vary the number of channels presented to the CRx denoted by  $N_{ch}$ . Using this filter, we can vary  $N_{ch}$  between 1 and 16, where the extreme cases correspond to fully filtered and fully colorless reception schemes, respectively.

In reception configuration (1), the frequency of the LO laser is swept to the center frequency of the channel desired to be selected out of the 16 available channels. However in configuration (2), the LO frequency is constantly set to channel 9 (channel of interest in this configuration) and the bandwidth of the tunable filter is set to control the number of out-of-band (OOB) WDM neighbors ( $N_{ch} - 1$ ) co-incident on the CRx with channel 9. In both configurations, the VOA sets the received power level per channel ( $P_{SIG}$ ) as desired prior to the CRx. At all received power levels, the voltage swing provided by the TIAs at the output of the CRx is maintained at a constant 320 mVpp (single-ended). Finally, the four electrical signals are sampled at 80 GSa/s using one Agilent DSOX96204Q real-time scope and stored for offline processing using a myriad of standard DSP algorithms to mitigate various impairments.

Offline processing starts by IQ power imbalance compensation and quadrature error correction using Gram-Schmidt orthogonalization, resampling to 2 samples per symbol, chromatic dispersion (CD) compensation in the frequency domain [1,5,6] and frequency offset removal using the periodogram method [32]. Polarization is then demultiplexed using a 31-tap butterfly equalizer whose taps are updated using the constant modulus algorithm (CMA) with a step size of  $1 \times 10^{-3}$  [1]. Phase noise was mitigated by a decision-directed phase locked loop (DD-PLL) [33]. After hard decision on a symbol-by-symbol basis, the achieved electrical SNR was evaluated and BER was finally calculated.

## 4.2 Experimental results and discussion

In this subsection, we present all experimental results obtained using the setup depicted in Fig. 3. In subsection 4.2.1, we show the results of reception configuration (1) in which fully colorless and preamplifierless strategy is employed. Next, subsection 4.2.2 presents all results collected on channel 9 employing reception configuration (2) where the EDFA and the tunable wavelength & bandwidth filter in the grey shaded box in Fig. 3 are inserted prior to the CRx. Using this configuration, various operating parameters such as the received signal power per channel ( $P_{SIG}$ ), LO power ( $P_{LO}$ ), number of channels ( $N_{ch}$ ) incident on the CRx, and distance ( $L$ ) are swept. Results collected from channel 9 include the SNR measured after offline DSP while sweeping the aforementioned parameters to evaluate the impact of each parameter on the performance of colorless CRx operation and to identify the dynamic range of the CRx for various number of channels. Based on the results, we also identify the key specifications of the CRx that are crucial for colorless operation. In subsection 4.2.3, we use the experimental SNR data at various operating parameters to fit the analytical SNR expression derived in section 3. The fitted SNR model is then used to predict the SNR at other operating parameters beyond our experimental capabilities, e.g. larger  $N_{ch}$ .

### 4.2.1 Configuration (1): BER for all channels at various distances using fully colorless and preamplifierless reception at either $-3$ dBm/ch or $-21$ dBm/ch

BERs of all 16 WDM channels were calculated and are plotted in Fig. 4 for 3200, 4480 and 4800 km transmission at two different  $P_{SIG}$  ( $-3$  and  $-21$  dBm per channel). All results in Fig. 4 are collected in the fully colorless and preamplifierless reception termed above by reception configuration (1). The LO power ( $P_{LO}$ ) was set to 15.5 dBm and its frequency was tuned to select each one of the 16 channels before data was acquired. Insets at the right of Fig. 4 also show the WDM spectra in back-to-back and after 3200 km transmission obtained using a 0.05 nm resolution bandwidth on the OSA. Throughout the manuscript, we assume  $3.8 \times 10^{-3}$  forward error correction (FEC) threshold, which is typical for the hard-decision FEC algorithm with 7% overhead defined in [34]. Then, if we carefully examine the BERs of all 16 channels, we can claim a 4800 km reach for all channels at  $P_{SIG}$  of  $-3$  dBm which

slightly decreases to 4160 km at  $-21$  dBm per channel. As will be explained in upcoming subsections, the good performance (reach) achieved by the CRx for fully colorless and preamplifierless reception with very low received signal power of  $-21$  dBm per channel is enabled by moderate CMRR and responsivity possessed by the CRx.

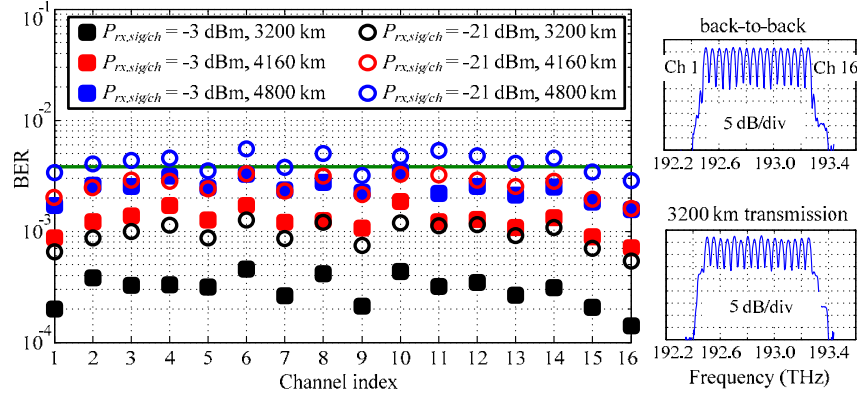


Fig. 4. BER for all WDM channels using fully colorless and preamplifierless reception at different transmission distances and at per channel received signal power of  $-3$  and  $-21$  dBm. Insets show the received WDM spectra in back-to-back and after 3200 km transmission where we observe a fairly flat spectrum due to the gain flattening waveshaper in the loop.

#### 4.2.2 Configuration (2): SNR of channel 9 when using a varying number of channels

Having evaluated the CRx colorless / preamplifierless operation for each channel across the spectrum, we now focus on channel 9 specifically. All measurements on channel 9 presented in the upcoming subsections, which involve sweeping various experimental parameters such as  $P_{LO}$ ,  $P_{SIG}$ ,  $N_{ch}$  and  $L$ , will use the SNR calculated after offline DSP instead of BER as the performance metric. The reason for using SNRs instead of BERs is that SNRs allow us to assess the performance quantitatively in back-to-back and short transmission distance scenarios when BERs are usually below  $10^{-5}$ . Evaluating BERs in this low-error regime would require acquiring and storing a number of symbols exceeding the memory of the real-time scope used. Also, later in this section, utilizing the experimental SNRs allows us to perform direct comparison with analytically predicted SNRs based on the derived SNR expression in section 3.

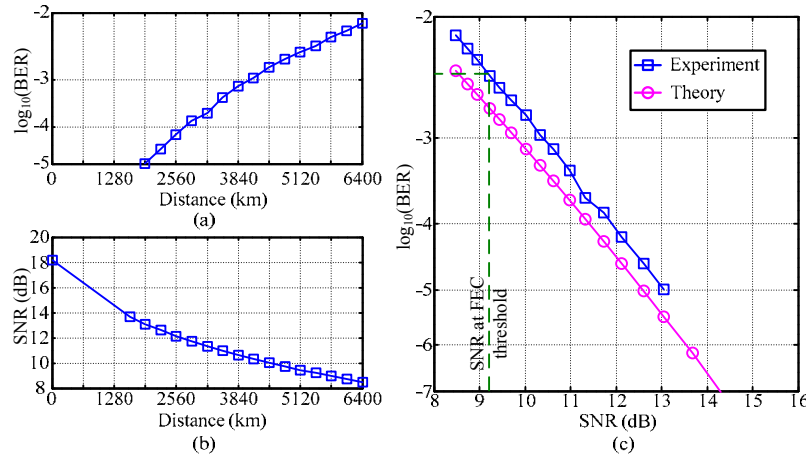


Fig. 5. Measurement results of channel 9: (a) BER versus transmission distance, (b) SNR evaluated after offline DSP versus distance, (c) BER versus SNR using both experimental results and theory where the experimental SNR corresponding to FEC threshold is marked.

Figure 5 shows the relationship between experimentally evaluated BER and SNR for channel 9. In Fig. 5(a), we plot the calculated BER on a double log scale versus the transmission distance whereas Fig. 5(b) shows the corresponding SNR evaluated at these distances. Using both curves, we plot in Fig. 5(c) the BER versus SNR relationship found experimentally. We find that a 9.2 dB SNR corresponds to the  $3.8 \times 10^{-3}$  FEC threshold which is 0.67 dB higher than the theoretical SNR of 8.53 dB at this BER level for 28 Gbaud QPSK assuming an ideal additive white Gaussian noise (AWGN) channel [35]. By means of Fig. 5(c), all SNR results that will be presented in the forthcoming subsections can be mapped into BER values in a straightforward manner.

#### 4.2.2.1 Impact of received signal power and number of channels presented to the CRx on the SNR of channel 9 at various distances and LO powers

From this point forward, the entire measurements are performed only for channel 9 in the WDM spectrum. In Figs. 6(a)–6(f), we show the SNR versus  $P_{SIG}$  at different LO powers of 15.5, 12, 9, 6, 3 and 0 dBm, respectively. In each subplot, we plot the SNR curves with different colors corresponding to various number of channels ( $N_{ch}$ ) presented to the CRx where  $N_{ch}$  is set to either 1, 5, 11 or 16 channels, ranging from fully filtered to colorless reception respectively. Also in each subplot, SNR curves measured at various transmission distances of 0, 1600, 3200 and 4800 km are plotted together where the top group of four curves always corresponds to the back-to-back case whereas the bottom set of curves represents the 4800 km transmission case. By examining Figs. 6(a)–6(f), we notice that the sweep range of  $P_{SIG}$  starts at –24 dBm for  $P_{LO} = 15.5$  and 12 dBm (see Figs. 6(a) and 6(b)), whereas for  $P_{LO} = 9, 6, 3$  and 0 dBm the sweep range of  $P_{SIG}$  had to be reduced to start at –21, –18, –15 and –12 dBm, respectively (see Figs. 6(c)–6(f)). The reason for increasing the lower end of the  $P_{SIG}$  sweep range for  $P_{LO} \leq 9$  dBm is to be able to achieve the fixed target voltage swing of 320 mVpp after the TIAs at the CRx output. For that reason, at each  $P_{LO} \leq 9$  dBm, the minimal value of the  $P_{SIG}$  sweep range was fixed to the least power level at which the TIAs could provide the 320 mVpp target swing when their respective gain was set to maximum (5 k $\Omega$  differential transimpedance  $Z_t$ ). Since for a fixed target voltage swing, the required  $Z_t$  for the TIAs is proportional to  $\sqrt{P_{LO}P_{SIG}}$ , we notice in Figs. 6(c)–6(f) that as  $P_{LO}$  is decreased by 3 dB going from one subfigure to the next, the starting point of the  $P_{SIG}$  sweep range (at maximum  $Z_t$ ) increases by 3 dB supporting the above proportionality.

Looking at the SNR variation with  $P_{SIG}$  throughout Figs. 6(a)–6(f), we notice that regardless of  $P_{LO}$ ,  $L$  and  $N_{ch}$ , the SNR improves as  $P_{SIG}$  is increased to an extent after which the SNR starts to decrease if  $P_{SIG}$  is further increased. This means that an optimum  $P_{SIG}$  exists for each  $P_{LO}$ ,  $L$ , and  $N_{ch}$ . Furthermore, if a certain target required SNR at a certain  $P_{LO}$ ,  $L$  and  $N_{ch}$  is to be achieved, one can specify a dynamic range for  $P_{SIG}$  within which the target SNR is at least guaranteed. It is noticeable that the dynamic range of  $P_{SIG}$  at a given  $L$  and  $P_{LO}$  decreases as  $N_{ch}$  is increased from 1 to 16 showing the impact of colorless reception. Finally, the dynamic range of  $P_{SIG}$  at a given  $L$  and  $N_{ch}$  is also found to decrease when  $P_{LO}$  is decreased.

The two reasons for the SNR degradation at the low and high ends of  $P_{SIG}$  are distinct. At high received signal power ( $P_{SIG} \sim 0$  dBm), the SNR degradation observed with a further increase of  $P_{SIG}$  is due to the residual SIG-SIG beat noise which is expressed by the last term in the denominator of Eq. (11). This SIG-SIG beat noise is proportional to  $N_{ch}P_{SIG}^2$  which explains why the SNR degrades as  $P_{SIG}$  is increased and why this degradation is more pronounced as more channels are presented to the CRx. In fact, we can re-write Eq. (11) by neglecting the thermal and shot noises at high  $P_{SIG}$  and dividing by  $P_{LO}P_{SIG}$ , which yields

$$SNR = \frac{2}{2C_1OSNR^{-1} + CMRR_{SIG}N_{ch}\beta \cdot LSR^{-1}}, \quad (12)$$

where  $LSR$  is the LO to signal power ratio at the CRx input. We can see from Eq. (12) that for a fixed OSNR, i.e. fixed distance, the SNR depends on the effective CMRR defined in

section 3,  $N_{ch}$  and  $LSR$ . If more channels are introduced to the CRx, the SNR degrades due to larger SIG-SIG beating from the OOB neighbors. Also, the impact of the SIG-SIG beat noise can be greatly reduced if high enough  $LSR$  is employed, which is also apparent in Fig. 6 by observing the impact of  $P_{LO}$  on the SNR difference between the cases of  $N_{ch} = 1$  and  $N_{ch} = 16$ , i.e. the SNR penalty due to colorless reception compared to filtered reception denoted by  $\Delta SNR_{1,16}$ , at a given  $L$  and at  $P_{SIG} = 0$  dBm.

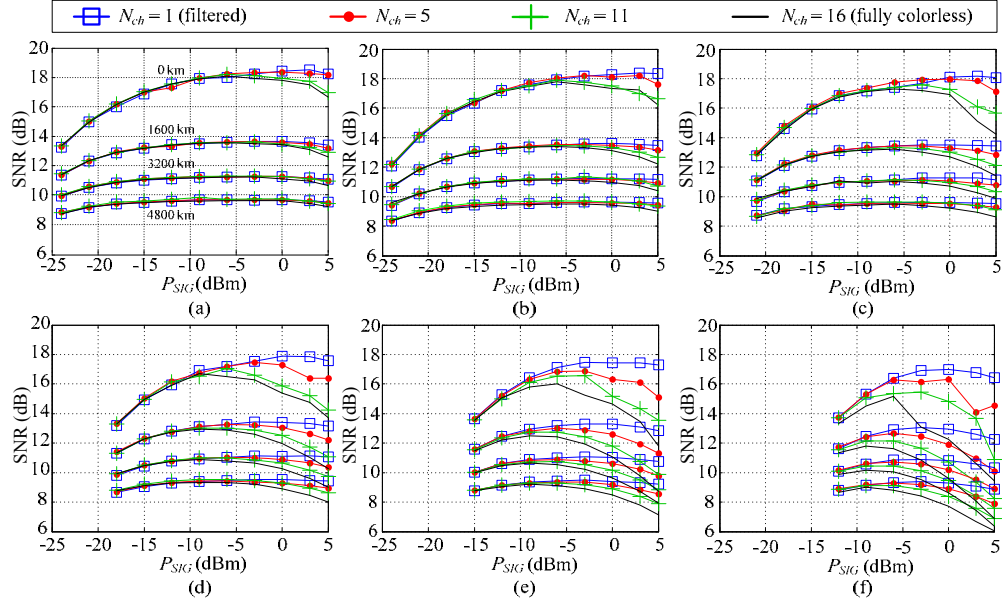


Fig. 6. SNR of channel 9 versus received signal power per channel  $P_{SIG}$  after 0, 1600, 3200 and 4800 km transmission with varying number of channels presented to the CRx at an LO power of: (a) 15.5 dBm, (b) 12 dBm, (c) 9 dBm, (d) 6 dBm, (e) 3 dBm, (f) 0 dBm. In each subfigure, different colors represent different number of channels  $N_{ch}$  according to the legend. Also, SNR evaluated after 0, 1600, 3200 and 4800 km transmission are shown in each subfigure where the top set of four curves in each subfigure is evaluated in back-to-back and the bottom set is after 4800 km transmission.

Since we are now interested in the high end of  $P_{SIG}$  and studying the impact of  $N_{ch}$  on SNR, we re-plot in Fig. 7 a portion of the results shown in Fig. 6 by focusing only on the SNR at  $P_{SIG} = 0$  dBm. Figures 7(a)–7(f) show the SNR after 0, 1600, 3200 and 4800 km transmission versus  $N_{ch}$  at LO powers from 15.5 dBm down to 0 dBm, all at  $P_{SIG} = 0$  dBm. This exactly corresponds to  $LSRs$  ranging from 15.5 dB to 0 dB. By examining Fig. 7 carefully, we notice that for  $LSR \geq 9$  dB, i.e.  $P_{LO} \geq 9$  dBm,  $\Delta SNR_{1,16}$  in Figs. 7(a)–7(c) is found to be  $< 1.2$  dB at any of the various distances travelled, which is a reasonably small degradation given the transceiver flexibility and hardware savings gained in an entirely colorless reception scheme. In fact, this 1.2 dB SNR penalty due to colorless reception is only pronounced in back-to-back at  $P_{LO} = 9$  dBm whereas  $\Delta SNR_{1,16}$  is less after transmission. This can be explained in light of the approximate SNR expression in Eq. (12) by noting that the OSNR decreases as  $L$  increases and hence the SIG-SIG beat term becomes less significant relative to the first term. On the other hand for  $LSR < 9$  dB,  $\Delta SNR_{1,16}$  in Figs. 7(d)–7(f) increases significantly where it becomes most apparent in Fig. 7(f) when  $LSR = 0$  dB. In view of Eq. (12), it should be finally noted that the SNR degradation due to colorless reception can be greatly reduced by developing coherent receivers with improved CMRRs which results in a better rejection for the SIG-SIG beating from the OOB channels.



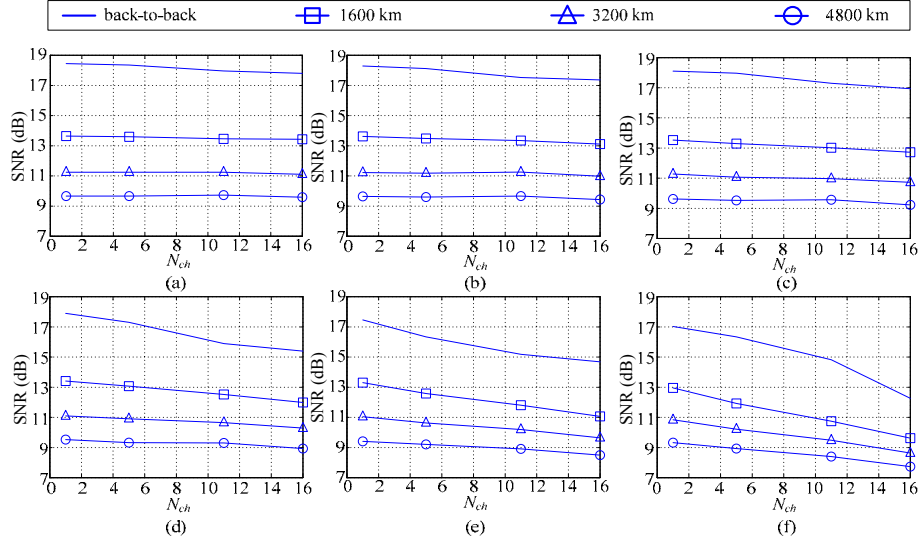


Fig. 7. SNR of channel 9 versus  $N_{ch}$  at  $P_{SIG} = 0$  dBm after 0, 1600, 3200 and 4800 km transmission at  $P_{LO}$  of (a) 15.5 dBm, (b) 12 dBm, (c) 9 dBm, (d) 6 dBm, (e) 3 dBm, (f) 0 dBm.

Looking back at Fig. 6 for low received signal powers ( $P_{SIG} \leq -12$  dBm), we notice that the SNR degrades quickly as  $P_{SIG}$  decreases and that the SNR is independent of  $N_{ch}$ . Referring back to the general SNR expression in Eq. (11), we re-write the expression by neglecting the SIG-SIG beat term for low  $P_{SIG}$  and dividing by  $P_{SIG}P_{LO}$ , which yields

$$SNR = \frac{2}{2c_1OSNR^{-1} + c_2 \cdot \frac{4eR_{LO}^{av}\Delta f}{P_{SIG}} + c_2 \cdot \frac{i_{TL4}^2\Delta f}{P_{LO}P_{SIG}}}, \quad (13)$$

where we neglected the signal contribution to the shot noise and kept only the LO shot noise term. In view of Eq. (13), we can easily explain the SNR trends at the low end of  $P_{SIG}$  in Fig. 6. First, it is clear that as  $P_{SIG}$  increases while  $P_{LO}$  is fixed, the SNR increases due to the second and third terms (shot and thermal noises) in the denominator of Eq. (13) being smaller which matches our observation in Fig. 6. In addition, we also observe in Fig. 6 that the impact of changing  $P_{SIG}$  is less pronounced as  $L$  increases which can be explained by the decrease in the OSNR with  $L$ , thus making the first term in the denominator of Eq. (13) larger compared to the second and third ones. Our next observation based on Eq. (13) is that increasing  $P_{LO}$  for a fixed  $P_{SIG}$  should also improve the SNR which goes along with the experimental results in Fig. 6. Comparing the impact of  $P_{SIG}$  and  $P_{LO}$  on the SNR in the low received signal power regime, we can observe in Fig. 6 that increasing  $P_{SIG}$  by 3 dB for a fixed  $P_{LO}$  results in a larger SNR improvement compared to increasing  $P_{LO}$  by 3 dB for a fixed  $P_{SIG}$ . As an example, if  $P_{SIG}$  is increased from  $-21$  to  $-18$  dBm at  $P_{LO} = 9$  dBm, the SNR improves by 1.68 dB whereas the improvement is 1.26 dB if  $P_{LO}$  increases from 9 to 12 dBm while keeping  $P_{SIG}$  at  $-21$  dBm. The observation that  $P_{SIG}$  has a slightly larger impact on the SNR compared to  $P_{LO}$  can also be explained in light of the denominator of Eq. (13) by noting that  $P_{SIG}$  affects both the second and third terms compared to  $P_{LO}$  impacting only one term. Next, we notice that the SNR in Eq. (13) is totally independent of  $N_{ch}$  at low  $P_{SIG}$  which agrees with Fig. 6. In order to further make this independence clear, we re-plot in Fig. 8 a portion of the results in Fig. 6 which are collected at  $P_{SIG} = -12$  dBm. Figures 8(a)–8(f) show the SNR after 0, 1600, 3200 and 4800 km transmission versus  $N_{ch}$  at LO powers from 15.5 dBm down to 0 dBm, all at low  $P_{SIG}$  of  $-12$  dBm. In Fig. 8, it is evident that  $N_{ch}$  has no impact on the SNR at either any distance or any  $P_{LO}$  at  $P_{SIG} = -12$  dBm.

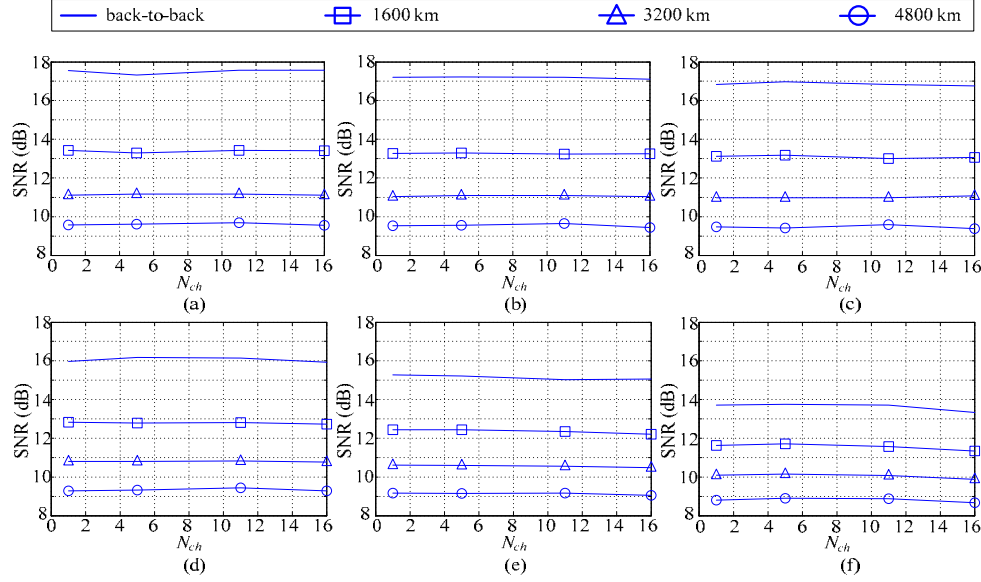


Fig. 8. SNR of channel 9 versus  $N_{ch}$  at  $P_{SIG} = -12$  dBm after 0, 1600, 3200 and 4800 km transmission at  $P_{LO}$  of (a) 15.5 dBm, (b) 12 dBm, (c) 9 dBm, (d) 6 dBm, (e) 3 dBm, (f) 0 dBm.

Finally, it should be also noted that the CRx responsivity is a key specification in this low  $P_{SIG}$  regime because according to Eq. (13) if all parameters stay the same while  $R_{SIG}$  and  $R_{LO}$  are increased, the SNR will consequently increase (note that  $c_2 \propto (R_{SIG}R_{LO})^{-1}$ ). Physically speaking, larger responsivities translate into larger photocurrents from the PDs relative to the fundamental CRx noise. Although the CRx used in our experiments possess a moderate responsivity due to relatively high coupling losses into the SiP chip, it still allows for good performance at low  $P_{SIG}$ . For example when  $P_{LO} = 12$  dBm, the SNR after 1600-4800 km transmission degrades by  $< 1$  dB when  $P_{SIG}$  decreases from 0 to  $-18$  dBm while providing the same output voltage swing using the TIA gain.

#### 4.2.2.2 Impact of LO power on the SNR of channel 9 at various distances and number of channels presented to the CRx for both regimes of high and low received signal power

In this subsection, we explicitly show the impact of the LO power on the SNR of channel 9. In Fig. 9, we re-plot a portion of the results shown in Fig. 6 where we show the SNR versus  $P_{LO}$  at various distances and number of channels presented to the CRx for both regimes of high and low received signal powers ( $P_{SIG} = 0$  and  $-15$  dBm, respectively). For the  $P_{SIG} = 0$  dBm case in Fig. 9(a), we observe how significant it is to choose a high LSR which greatly reduces the SNR penalty due to colorless reception. For example, changing the LSR from 0 to 12 dB reduces  $\Delta\text{SNR}_{1,16}$  from 1.5 to 4.7 dB (for distances travelled from 4800 to 0 km) to 0.1-0.65 dB. This agrees with Eq. (12) as discussed in the previous subsection. Moving to Fig. 9(b) when  $P_{SIG} = -15$  dBm, we notice that increasing  $P_{LO}$  improves the SNR and that the SNR is independent of  $N_{ch}$  which agrees with Eq. (13). As mentioned in section 3, the LO-LO beat noise was not observed throughout all experimental data because the RIN of our lasers is below  $-145$  dB/Hz. However, it is noteworthy that as  $P_{LO}$  is increased beyond 15.5 dBm (maximum output power from our ECLs) at  $P_{SIG} = -15$  dBm (see Fig. 9(b)), the LO-LO beat noise should eventually lead to SNR degradation.

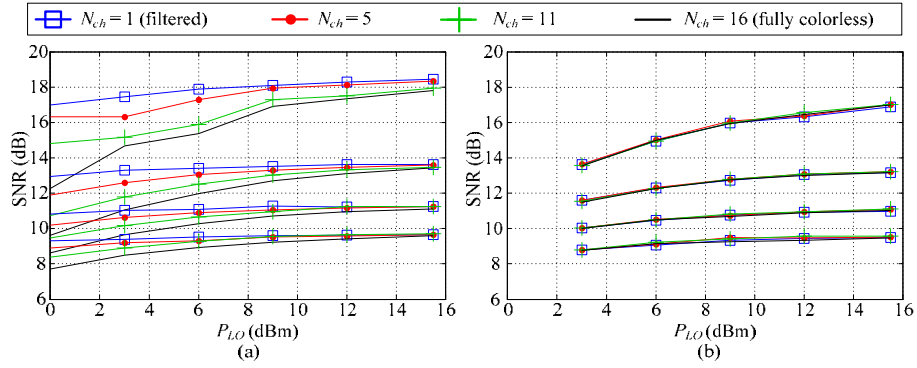


Fig. 9. SNR of channel 9 versus  $P_{LO}$  after 0, 1600, 3200 and 4800 km transmission at various  $N_{ch}$  and at  $P_{SIG}$  of: (a) 0 dBm, (b) -15 dBm.

#### 4.2.2.3 Two dimensional (2-D) plots of SNR of channel 9 versus LO power and received signal power at different distances in case of 1 (filtered) and 16 channels (colorless)

In this subsection, we re-present the experimental data of Fig. 6 corresponding to the extreme cases of  $N_{ch} = 1$ , i.e. filtered operation and  $N_{ch} = 16$ , i.e. fully colorless operation. Here, we present the SNR data as two dimensional (2-D) plots versus both  $P_{SIG}$  and  $P_{LO}$  as the two independent variables being swept. Figure 10 depicts these 2-D plots where different SNR values are encoded into different colors according to the color bars beside each subfigure (red representing higher SNR whereas blue representing smaller SNR). In all Figs. 10(a)–10(h), the small  $\mathbf{x}$ 's mark the positions of experimental data points across the 2-D space ( $P_{SIG}$ ,  $P_{LO}$ ). All values between those points are evaluated using linear interpolation using the two nearest experimental data points resulting in continuous and smooth color-coded surfaces. The four rows of subfigures in Fig. 10 represent data after 0, 1600, 3200, and 4800 km transmission, respectively, whereas the left column of subfigures represent the filtered case ( $N_{ch} = 1$ ) and the right column represent the colorless case ( $N_{ch} = 16$ ). We should also notice that each pair of subfigures in any row share the same SNR color bar to ease the comparison within each row between the filtered and colorless scenarios. Also, we observe in all subfigures a white space at the bottom left corner where no surface is plotted. This range of ( $P_{SIG}$ ,  $P_{LO}$ ) has no experimental data since the target voltage swing of 320 mVpp could not be achieved within this range when both  $P_{SIG}$  and  $P_{LO}$  are small.

Also, we plot in each subfigure (if applicable) a black contour line corresponding to the parameters ( $P_{SIG}$ ,  $P_{LO}$ ) that achieve an SNR of 9.2 dB (FEC threshold). If we now compare Figs. 10(g) and 10(h) in the last row, we notice that the operating range where error-free operation is achieved, i.e. when  $\text{SNR} > 9.2$  dB which is the area above the contour, is tighter in case of  $N_{ch} = 16$  compared to  $N_{ch} = 1$  due to the residual SIG-SIG self beat noise impact in the case of colorless reception which degrades the SNR as  $P_{SIG}$  increases and  $P_{LO}$  decreases. Within the operating range, we notice that for a fixed  $P_{LO}$ , there is a dynamic range for  $P_{SIG}$  within which error-free operation is possible and that this dynamic range gets wider as  $P_{LO}$  increases. Generally, the SNR degradation observed in the left edge of the surfaces in Figs. 10(a)–10(h) is due to the fundamental receiver shot and thermal noises. On the other hand, we notice a SNR degradation in the bottom right corner (where the  $LSR$  is smallest) of all subfigures in the right column representing the colorless scenario, due to the residual SIG-SIG self-beat noise due to neighboring WDM channels in this case. In fact, one should also expect SNR degradation near the top right corner of all subfigures due to saturation effects when both  $P_{SIG}$  and  $P_{LO}$  are large. In this case, the TIAs may get overloaded leading to nonlinear distortion of the signal which in turn degrades the SNR. From a system design perspective, the TIA overload problem is governed by two important parameters namely the

maximum single-ended DC current ( $I_{DC}$ ) and the peak-to-peak differential AC current ( $I_{ACppd}$ ), which are calculated similar to [16] as follows

$$I_{DC} = R_{LO}P_{LO} + N_{ch}R_{SIG}P_{SIG}, \quad (14)$$

$$I_{ACppd} = 8\sqrt{R_{LO}P_{LO} \cdot PAPR \cdot R_{SIG}P_{SIG}}, \quad (15)$$

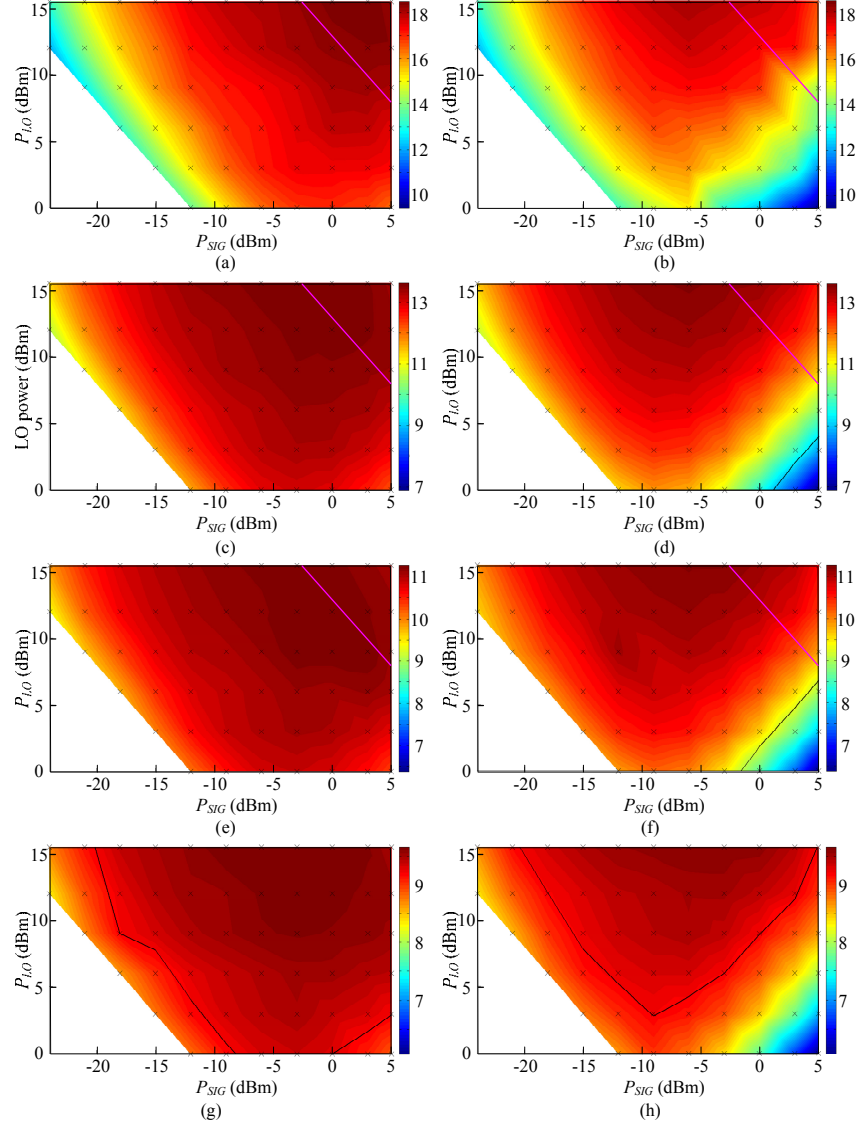


Fig. 10. Color coded 2-D plots of SNR versus both  $P_{SIG}$  and  $P_{LO}$  for (a) back-to-back and  $N_{ch} = 1$ , (b) back-to-back and  $N_{ch} = 16$ , (c) 1600 km transmission and  $N_{ch} = 1$ , (d) 1600 km transmission and  $N_{ch} = 16$ , (e) 3200 km transmission and  $N_{ch} = 1$ , (f) 3200 km transmission and  $N_{ch} = 16$ , (g) 4800 km transmission and  $N_{ch} = 1$ , and (h) 4800 km transmission and  $N_{ch} = 16$ .

where  $PAPR$  is the peak-to-average power ratio of the photocurrent of one WDM channel which depends on the residual CD and polarization orientation [16]. If those two currents calculated in Eqs. (14) and (15) are guaranteed to be below the maximum ratings of the TIA, TIA saturation will be avoided and linear operation will be achieved. In our experiment, the

TIA had maximum ratings of 4 mA and 3 mA for  $I_{DC}$  and  $I_{ACppd}$ , respectively. Regarding DC saturation, if we use the effective responsivities of our CRx which are 0.025 and 0.029 A/W for the signal and LO ports, respectively, we can infer from Eq. (14) that for the experimental point with the largest  $P_{LO}$ ,  $P_{SIG}$  and  $N_{ch}$  in Fig. 10, i.e. when  $P_{LO} = 15.5$  dBm,  $P_{SIG} = 5$  dBm and  $N_{ch} = 16$ ,  $I_{DC}$  will be 2.27 mA which is below 4 mA, meaning that no DC saturation has occurred in our experiment and that the results in Fig. 10 are not affected by the TIA DC overload. On the other hand, the AC overload problem affects a portion of our experimental data. If we use a  $PAPR$  of 10 dB [36] and the CRx responsivities defined above, we can use Eq. (15) to evaluate  $(P_{LO}, P_{SIG})$  that corresponds to  $I_{ACppd} = 3$  mA which yields the magenta lines plotted in Figs. 10(a)–10(h) near the top right corner of each subfigure. This means that the experimental points above these contours were affected by TIA AC saturation whereas all points lying below these lines were not impacted by AC saturation and the TIAs were in the linear regime of operation. Finally, it is noteworthy that the two currents calculated according to Eqs. (14) and (15) are not the only key parameters that should be considered when assessing TIA saturation. In fact, one should also consider the common mode AC current (which is dependent on  $N_{ch}$ ). One can actually evaluate the single-ended AC current, i.e. before subtraction that takes place inside the TIA, which should include both the common mode and differential AC contributions. However, the TIA specification regarding the maximum common mode AC current was not available and hence, was not considered.

#### 4.2.3 Verification of experimental results using the analytical SNR model

In this subsection, the goal is to verify the match between the experimental data presented in the preceding subsections and the behavior predicted by the analytical SNR model given by Eq. (11). In order to do so, the analytical SNR model in Eq. (11) is fitted to the experimental data. We first re-write Eq. (11) after re-expressing the denominator which represents the various noise sources as follows

$$SNR = \frac{P_{LO}P_{SIG}}{\alpha_1 P_{LO}P_{SIG} + \alpha_2 N_{loops} P_{LO}P_{SIG} + \alpha_3 + \alpha_4 (P_{LO} + N_{ch} P_{SIG}) + \alpha_5 N_{ch} P_{SIG}^2}, \quad (16)$$

where  $\alpha_1, \alpha_2, \dots, \alpha_5$  are the coefficients that need to be estimated in order to fit the model in Eq. (16) to the experimental data. In fact, the first two terms in the denominator of Eq. (16) represent the LO beating with the noise coming along with the received signal which was represented by the first term (LO-ON beating) in the denominator of Eq. (11). Here, we split this term into two terms representing the LO beating with the noise accompanying the received signal in back-to-back and transmission scenarios, respectively. The reason to add a noise accompanying the signal in the back-to-back case is to take into account the noise due to the transmitter. This noise from the transmitter side impacts the signal even without transmission and originates from the booster EDFA, RF drivers of the IQ modulator, etc. Hence, the  $\alpha_1$  term in Eq. (16) is independent of the transmission distance. On the other hand, the  $\alpha_2$  term represents the LO beating with the incoming optical noise due to both ASE noise of the in-line EDFAs and NL-induced noise after dispersion uncompensated transmission. According to [27], as the number of WDM channels increases and the channel spacing gets smaller, i.e. more dense spectrum, the NL-induced noise accumulation along the link is approximately linear with the number of spans which corresponds to summing incoherently the powers of NL noise contributions from various spans. In our experiment, we always had 16 WDM channels with 50 GHz spacing propagating along the link which results in NL accumulation approximately proportional to  $N_{spans}^{1.06}$  [27], which is very close to being linear. Hence, both the ASE and NL-induced AWGNs can be safely assumed to scale linearly with the number of spans, and consequently, with the number of loops in the recirculating loop,  $N_{loops}$ . Next, by carefully comparing the first noise term in Eq. (11) with the first two noise terms in Eq. (16), we notice that the first noise term in Eq. (11) is expressed in terms of

the product  $P_{LO}P_{ON}$  whereas in Eq. (16), we make use of the proportionality between  $P_{ON}$  and  $P_{SIG}$  for a fixed OSNR and write both the  $\alpha_1$  and  $\alpha_2$  terms in terms of  $P_{LO}P_{SIG}$  instead, i.e. the inverses of the OSNRs in back-to-back and after one loop transmission are imbedded into  $\alpha_1$  and  $\alpha_2$ , respectively. We should note that the launch power, which affects  $P_{ON}$  by changing the power of the NL-induced noise contribution, was kept constant throughout the experiment. In fact,  $P_{SIG}$  in Eq. (16) denotes the received signal power (not the launch power) that was swept using the VOA prior to the CRx after NL accumulation already happened along the fiber. In addition, it is noteworthy that the number of WDM channels propagating along the link in our experiment was also kept constant at 16, whereas the number of channels presented to the CRx, denoted by  $N_{ch}$  in Eq. (16), was swept using the tunable bandwidth optical filter at the end of the link prior to the CRx. Hence, the NL-induced noise along the link in our experiment was constant. Next, the  $\alpha_3$  term represents the thermal noise which is assumed independent of  $P_{LO}$  and  $P_{SIG}$ . Then, the  $\alpha_4$  term is due to the shot noise including both the LO and SIG contributions. It is noteworthy that both  $\alpha_3$  and  $\alpha_4$  depend on the responsivity of the CRx beside various other parameters. Finally, the  $\alpha_5$  term represents the residual SIG-SIG beating and hence is proportional to  $N_{ch}P_{SIG}^2$  where  $\alpha_5$  includes the impact of the effective CMRR of the signal port and the scaling factor  $\beta$ .

The next step is to estimate  $\alpha_1, \alpha_2, \dots, \alpha_5$  in Eq. (16) using the experimental data plotted in Fig. 6. For the purpose of fitting the model, we use only the experimental data obtained after transmission corresponding to  $N_{loops}$  equal to 5, 10 and 15 because at these distances, the scaling factor  $\beta$  saturates to a constant value of 0.55 (see appendix B) and hence  $\alpha_5$  can be assumed constant. Since we have many SNR data points at various operating parameters namely,  $P_{LO}$ ,  $P_{SIG}$ ,  $N_{ch}$  and  $N_{loops}$ , estimating the coefficients  $\alpha_1, \alpha_2, \dots, \alpha_5$  requires solving an over-determined system. In order to do so, we use the linear least-squares method where the following two vectors and matrix are formed

$$\mathbf{a} = \begin{bmatrix} \alpha_1 \\ \vdots \\ \alpha_5 \end{bmatrix}, \quad \mathbf{y} = \begin{bmatrix} P_{LO_1}P_{SIG_1}/SNR_1 \\ \vdots \\ P_{LO_m}P_{SIG_m}/SNR_m \end{bmatrix}, \quad \mathbf{X} = \begin{bmatrix} P_{LO_1}P_{SIG_1} & N_{loops_1}P_{LO_1}P_{SIG_1} & 1 & P_{LO_1} + N_{ch_1}P_{SIG_1} & N_{ch_1}P_{SIG_1}^2 \\ \vdots & \vdots & \vdots & \vdots & \vdots \\ P_{LO_m}P_{SIG_m} & N_{loops_m}P_{LO_m}P_{SIG_m} & 1 & P_{LO_m} + N_{ch_m}P_{SIG_m} & N_{ch_m}P_{SIG_m}^2 \end{bmatrix},$$

where  $m$  is the number of data points. Using the least-squares method, an estimate  $\hat{\mathbf{a}}$  for the coefficients  $\mathbf{a}$  is computed such that  $\|\mathbf{a} - \hat{\mathbf{a}}\|^2$  is minimized and will be on the form [37]

$$\hat{\mathbf{a}} = (\mathbf{X}^T \mathbf{X})^{-1} \mathbf{X}^T \mathbf{y}, \quad (17)$$

where  $\|\mathbf{x}\|$  denotes the norm of a vector  $\mathbf{x}$ .

By plugging the estimated coefficients from Eq. (17) into the SNR model of Eq. (16), we now have a known analytical SNR model that can be employed to either verify the experimental data or evaluate the SNR at other operating conditions, e.g. another  $N_{ch}$ . Figure 11 shows a comparison between the experimental SNR data and the evaluated SNR data from the fitted analytical model where the SNR is plotted against  $P_{SIG}$  for various transmission distances. Figures 11(a) and 11(b) present the data when  $P_{LO}$  is set to 12 dBm and  $N_{ch}$  is 1 and 16, respectively whereas Figs. 11(c) and 11(d) present the data when  $P_{LO}$  is set to 3 dBm and  $N_{ch}$  is 1 and 16, respectively. In obtaining Fig. 11, we performed two least-squares fits of the SNR model: one for the back-to-back case and one for the transmission case, since  $\alpha_5$  is expected to be different in both scenarios. The reason for the expected difference of  $\alpha_5$

between the two scenarios is that  $\alpha_5$  includes the effect of the scaling factor  $\beta$  which is dependent on the amount of CD (see appendix B for more details on the scaling factor  $\beta$ ) and hence fitting the SNR model is done for the back-to-back data and transmitted data separately. Indeed,  $\alpha_5$  found from fitting the model to the transmitted data was 1.74 times larger than the fitted  $\alpha_5$  using the back-to-back data. This ratio matches well the expected value based on the theory in appendix B (see Fig. 13) if we use  $\beta$  of 0.55 for the transmitted data and  $\beta$  of 0.316 for the back-to-back data assuming the worst case polarization orientation of the received signal ( $45^\circ$  relative to the PBS of the CRx). Furthermore, we should anticipate that  $\alpha_5$  is the same for all transmitted data since  $\beta$  saturates quickly to a value of 0.55 when the residual CD is more than 3 ns/nm (see Fig. 13 in appendix B). Looking back at Fig. 11, we notice a good agreement between the SNR curves derived from the model compared to the experimental curves which verifies both the validity of the proposed model in Eq. (16) and the accuracy of the experimental data.

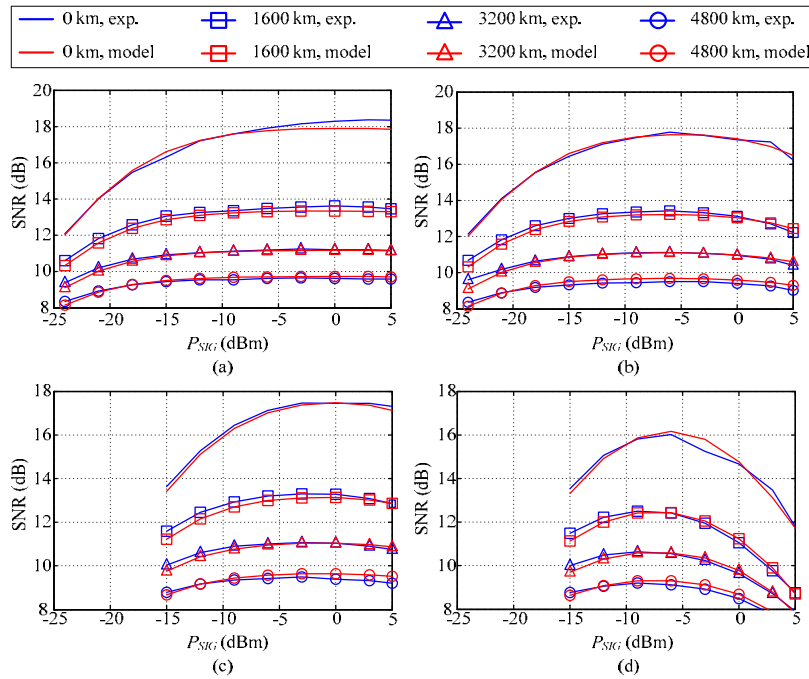


Fig. 11. SNR versus  $P_{SIG}$  comparing both experimental data points with the points evaluated from the fitted SNR analytical model after 0, 1600, 3200 and 4800 km at the following operating conditions: (a)  $P_{LO} = 12$  dBm and  $N_{ch} = 1$ , (b)  $P_{LO} = 12$  dBm and  $N_{ch} = 16$ , (c)  $P_{LO} = 3$  dBm and  $N_{ch} = 1$ , and (d)  $P_{LO} = 3$  dBm and  $N_{ch} = 16$ .

Besides the agreement between the model and the experimental SNR data, we can also use the estimated value of  $\alpha_5$  (in case of transmitted data) to calculate  $\overline{CMRR}_{SIG}$  assuming  $\beta = 0.55$  which can be easily done by comparing the last term in the denominators of Eqs. (11) and (16). We found that  $\overline{CMRR}_{SIG}$  obtained from the fitted coefficient is  $-19$  dB. In order to verify this value, we used the analytical definition of  $\overline{CMRR}_{SIG}$  presented below Eq. (11) in section 3 in addition to the CMRR versus frequency curves obtained via characterization of the CRx which were depicted in Fig. 2(a) of section 2. The value found through the analytical expression of  $\overline{CMRR}_{SIG}$  was  $-17.5$  dB which is in good agreement with the one obtained from fitting.



Next, we make use of the SNR model found in Eq. (16) to predict the SNR performance if the same CRx is used in operating conditions different from those of our experiment. For example, we use the model to predict the performance when the number of WDM channels co-incident on the CRx is larger than 16. In Fig. 12, we plot the SNR versus  $N_{ch}$  after 0, 1600, 3200 and 4800 km transmission for both the model and experiment. It can be observed that the sweep range of  $N_{ch}$  is limited to 16 in case of the experimental data whereas we employ the analytical model to predict the SNR if the CRx is used for colorless reception when  $N_{ch}$  is up to 80. In Figs. 12(a) and 12(b), a high  $P_{LO}$  of 12 dBm is chosen and  $P_{SIG}$  is set to 0 and -12 dBm, respectively whereas in Figs. 12(c) and 12(d) a low  $P_{LO}$  of 3 dBm is chosen and  $P_{SIG}$  is set to 0 and -12 dBm, respectively. If we compare Figs. 12(a)–12(d), we notice that the impact of increasing  $N_{ch}$  on the SNR degradation is the most in Fig. 12(c) where the residual SIG-SIG beat noise has the largest impact for small  $P_{LO}$  and high  $P_{SIG}$ , i.e. small  $LSR$ . For example, the SNR after 1600 km transmission degrades by nearly 6 dB as  $N_{ch}$  changes from 1 to 80. On the other hand, we observe no impact from varying  $N_{ch}$  on the SNR performance in Fig. 12(b) when  $P_{LO} = 12$  dBm and  $P_{SIG} = -12$  dBm. In fact, the model allows us to predict error free operation (SNR > 9.2 dB) after 4800 km transmission when  $N_{ch} = 80$ . In order to verify that our SNR predictions when  $N_{ch} = 80$  are correct from the TIA saturation perspective, we also use Eqs. (14) and (15) to verify if  $I_{DC}$  and  $I_{ACppd}$  are going to be below the TIA ratings. Indeed, if we plug the largest  $P_{SIG}$  and  $P_{LO}$  used in Fig. 12 into Eqs. (14) and (15), i.e. 0 dBm and 12 dBm respectively, and use  $N_{ch} = 80$ , we obtain  $I_{DC} = 2.43$  and  $I_{ACppd} = 2.69$  mA which are below the TIA maximum ratings. We finally conclude that all SNR points drawn from the model in Fig. 12 are within the linear regime of operation of the TIAs.

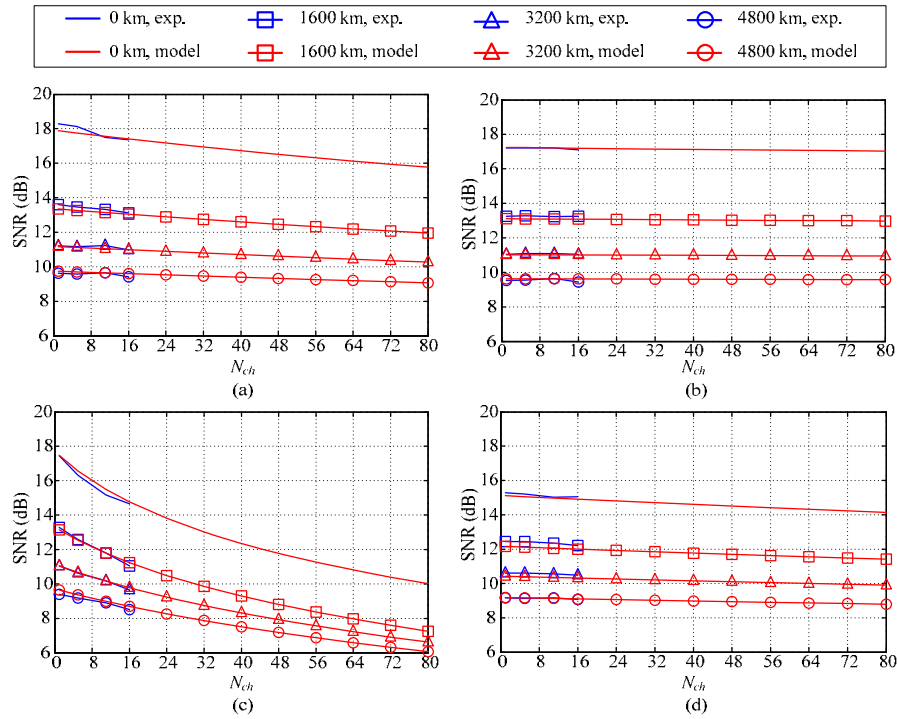


Fig. 12. SNR versus  $N_{ch}$  comparing the experimental data points with the points evaluated from the fitted SNR analytical model after 0, 1600, 3200 and 4800 km at the following operating conditions: (a)  $P_{LO} = 12$  dBm and  $P_{SIG} = 0$  dBm, (b)  $P_{LO} = 12$  dBm and  $P_{SIG} = -12$  dBm, (c)  $P_{LO} = 3$  dBm and  $P_{SIG} = 0$  dBm, and (d)  $P_{LO} = 3$  dBm and  $P_{SIG} = -12$  dBm.



## 5. Conclusion

In this paper, we present a comprehensive theoretical and experimental study of the performance of a SiP integrated balanced CRx when employed for colorless reception in a WDM setup. The layout of the CRx chip is depicted and characterization results of its parameters are shown. Then, an analytical SNR expression of the output photocurrent is derived rigorously while pinpointing noise sources in a colorless scheme. Next, experimental results are presented where  $16 \times 112$  Gbps PDM-QPSK WDM channels are used. We study the impact of varying system parameters on the performance of colorless reception. Results show that the LO beating with incoming optical noise including ASE and NL-induced noises is a dominant noise source regardless of the received signal power. In addition, we identify the SIG-SIG beating due to OOB WDM channels as an additional important noise source in the regime of high received signal power. On the other hand, thermal and shot noises have a significant impact on SNR in the regime of low received signal power. In addition, we conclude that the CMRR and sensitivity are two important CRx specifications that impact the performance at high and low received signal power regimes, respectively. Finally, an excellent match between experimental and analytical SNRs is proven. After fitting the SNR model, we conclude that the SiP CRx is capable of colorless operation with a WDM spectrum comprising 80 channels as long as the LO-to-signal power ratio is properly set.

## 6. Appendix A: Derivation of ACFs, PSDs and powers of various terms in the differential photocurrent

In this appendix, we derive the time-averaged ACFs of all terms in the total differential photocurrent given by Eq. (7) from which the PSDs are evaluated through Fourier transformation (FT). Then, the PSDs derived are integrated over frequency to calculate the powers required to evaluate the SNR according to Eq. (10). We divide the appendix into four subsections which are laid out for different beating terms of the differential photocurrent given in Eq. (7).

### 6.1 Derivation of ACF, PSD and power of the LO-SIG and LO-ON beating terms in the differential photocurrent

We start by neglecting the effect of the impulse responses of  $h^P(t)$  and  $h^N(t)$ . However, we will later modify the final result derived to include their impact. The time averaged ACF of the LO-SIG term in the differential photocurrent in Eq. (7) can be calculated starting from the definition of the ACF of  $\Delta i_{LO-SIG}(t)$ , obtained from the difference between the LO-SIG terms in the  $P$  and  $N$  photocurrents in Eqs. (5) and (6), yielding

$$\begin{aligned} \bar{G}_{\Delta i_{LO-SIG}}(\tau) &= \overline{\Delta i_{LO-SIG}(t) \Delta i_{LO-SIG}(t-\tau)} \\ &= R_{SIG,s}^P R_{LO,s}^P \overline{\left\{ \text{Re}\left\{ \tilde{E}_{SIG,s}(t) \tilde{E}_{LO}^*(t) e^{j2\pi\Delta\nu t} \right\} \cdot \text{Re}\left\{ \tilde{E}_{SIG,s}(t-\tau) \tilde{E}_{LO}^*(t-\tau) e^{j2\pi\Delta\nu(t-\tau)} \right\} \right\}} \\ &\quad + R_{SIG,s}^N R_{LO,s}^N \overline{\left\{ \text{Re}\left\{ \tilde{E}_{SIG,s}(t-\delta) \tilde{E}_{LO}^*(t-\delta) e^{j2\pi\Delta\nu(t-\delta)} \right\} \cdot \text{Re}\left\{ \tilde{E}_{SIG,s}(t-\tau-\delta) \tilde{E}_{LO}^*(t-\tau-\delta) e^{j2\pi\Delta\nu(t-\tau-\delta)} \right\} \right\}} \\ &\quad + \sqrt{R_{SIG,s}^P R_{LO,s}^P R_{SIG,s}^N R_{LO,s}^N} \overline{\left\{ \text{Re}\left\{ \tilde{E}_{SIG,s}(t) \tilde{E}_{LO}^*(t) e^{j2\pi\Delta\nu t} \right\} \cdot \text{Re}\left\{ \tilde{E}_{SIG,s}(t-\tau-\delta) \tilde{E}_{LO}^*(t-\tau-\delta) e^{j2\pi\Delta\nu(t-\tau-\delta)} \right\} \right\}} \\ &\quad + \sqrt{R_{SIG,s}^P R_{LO,s}^P R_{SIG,s}^N R_{LO,s}^N} \overline{\left\{ \text{Re}\left\{ \tilde{E}_{SIG,s}(t-\delta) \tilde{E}_{LO}^*(t-\delta) e^{j2\pi\Delta\nu(t-\delta)} \right\} \cdot \text{Re}\left\{ \tilde{E}_{SIG,s}(t-\tau) \tilde{E}_{LO}^*(t-\tau) e^{j2\pi\Delta\nu(t-\tau)} \right\} \right\}}. \end{aligned}$$

Using the relation in Eq. (4) to express the product of two real parts and also realizing that the terms having  $e^{j2\pi\Delta\nu(2t-\tau)}$  cancel after time averaging as in [29], we arrive at

$$\begin{aligned}
\bar{\Gamma}_{\Delta f_{LO-SIG}}(\tau) = & \frac{1}{2} R_{SIG,s}^P R_{LO,s}^P \text{Re} \left\{ \overline{\tilde{E}_{SIG,s}(t) \tilde{E}_{SIG,s}^*(t-\tau) \tilde{E}_{LO}(t) \tilde{E}_{LO}^*(t-\tau)} e^{j2\pi\Delta f\tau}} \right\} \\
& + \frac{1}{2} R_{SIG,s}^N R_{LO,s}^N \text{Re} \left\{ \overline{\tilde{E}_{SIG,s}(t-\delta) \tilde{E}_{SIG,s}^*(t-\tau-\delta) \tilde{E}_{LO}(t-\delta) \tilde{E}_{LO}^*(t-\tau-\delta)} e^{j2\pi\Delta f\tau}} \right\} \\
& + \frac{1}{2} \sqrt{R_{SIG,s}^P R_{LO,s}^P R_{SIG,s}^N R_{LO,s}^N} \text{Re} \left\{ \overline{\tilde{E}_{SIG,s}(t) \tilde{E}_{SIG,s}^*(t-\tau-\delta) \tilde{E}_{LO}(t) \tilde{E}_{LO}^*(t-\tau-\delta)} e^{j2\pi\Delta f(\tau+\delta)}} \right\} \\
& + \frac{1}{2} \sqrt{R_{SIG,s}^P R_{LO,s}^P R_{SIG,s}^N R_{LO,s}^N} \text{Re} \left\{ \overline{\tilde{E}_{SIG,s}(t-\delta) \tilde{E}_{SIG,s}^*(t-\tau) \tilde{E}_{LO}(t-\delta) \tilde{E}_{LO}^*(t-\tau)} e^{j2\pi\Delta f(\tau-\delta)}} \right\}.
\end{aligned} \tag{18}$$

Then, if use the statistical independence between the LO and signal fields, we obtain

$$\begin{aligned}
\bar{\Gamma}_{\Delta f_{LO-SIG}}(\tau) = & \frac{1}{2} R_{SIG,s}^P R_{LO,s}^P \text{Re} \left\{ \bar{\Gamma}_{\tilde{E}_{SIG}}(\tau) \Gamma_{\tilde{E}_{LO}}^*(\tau) e^{j2\pi\Delta f\tau} \right\} \\
& + \frac{1}{2} R_{SIG,s}^N R_{LO,s}^N \text{Re} \left\{ \bar{\Gamma}_{\tilde{E}_{SIG}}(\tau) \Gamma_{\tilde{E}_{LO}}^*(\tau) e^{j2\pi\Delta f\tau} \right\} \\
& + \frac{1}{2} \sqrt{R_{SIG,s}^P R_{LO,s}^P R_{SIG,s}^N R_{LO,s}^N} \text{Re} \left\{ \bar{\Gamma}_{\tilde{E}_{SIG}}(\tau+\delta) \Gamma_{\tilde{E}_{LO}}^*(\tau+\delta) e^{j2\pi\Delta f(\tau+\delta)} \right\} \\
& + \frac{1}{2} \sqrt{R_{SIG,s}^P R_{LO,s}^P R_{SIG,s}^N R_{LO,s}^N} \text{Re} \left\{ \bar{\Gamma}_{\tilde{E}_{SIG}}(\tau-\delta) \Gamma_{\tilde{E}_{LO}}^*(\tau-\delta) e^{j2\pi\Delta f(\tau-\delta)} \right\}.
\end{aligned} \tag{19}$$

The first term in Eq. (19) follows directly from the first term in Eq. (18) after using the statistical independence between the LO and signal fields. However, the second, third and fourth terms are each obtained as follows

$$\begin{aligned}
\overline{\tilde{E}_{SIG,s}(t-\delta) \tilde{E}_{SIG,s}^*(t-\tau-\delta) \tilde{E}_{LO}(t-\delta) \tilde{E}_{LO}^*(t-\tau-\delta)} &= \overline{\tilde{E}_{SIG,s}(t-\delta) \tilde{E}_{SIG,s}^*(t-\tau-\delta)} \cdot \overline{\tilde{E}_{LO}(t-\delta) \tilde{E}_{LO}^*(t-\tau-\delta)} \\
&= \overline{\Gamma_{\tilde{E}_{SIG}}(t-\delta, \tau)} \cdot \Gamma_{\tilde{E}_{LO}}^*(\tau) \\
&= \bar{\Gamma}_{\tilde{E}_{SIG}}(\tau) \cdot \Gamma_{\tilde{E}_{LO}}^*(\tau), \\
\overline{\tilde{E}_{SIG,s}(t) \tilde{E}_{SIG,s}^*(t-\tau-\delta) \tilde{E}_{LO}(t) \tilde{E}_{LO}^*(t-\tau-\delta)} &= \overline{\tilde{E}_{SIG,s}(t) \tilde{E}_{SIG,s}^*(t-\tau-\delta)} \cdot \overline{\tilde{E}_{LO}(t) \tilde{E}_{LO}^*(t-\tau-\delta)} \\
&= \overline{\Gamma_{\tilde{E}_{SIG}}(t, \tau+\delta)} \cdot \Gamma_{\tilde{E}_{LO}}^*(\tau+\delta) \\
&= \bar{\Gamma}_{\tilde{E}_{SIG}}(\tau+\delta) \cdot \Gamma_{\tilde{E}_{LO}}^*(\tau+\delta), \\
\overline{\tilde{E}_{SIG,s}(t-\delta) \tilde{E}_{SIG,s}^*(t-\tau) \tilde{E}_{LO}(t-\delta) \tilde{E}_{LO}^*(t-\tau)} &= \overline{\tilde{E}_{SIG,s}(t-\delta) \tilde{E}_{SIG,s}^*(t-\tau)} \cdot \overline{\tilde{E}_{LO}(t-\delta) \tilde{E}_{LO}^*(t-\tau)} \\
&= \overline{\Gamma_{\tilde{E}_{SIG}}(t-\delta, \tau-\delta)} \cdot \Gamma_{\tilde{E}_{LO}}^*(\tau-\delta) \\
&= \bar{\Gamma}_{\tilde{E}_{SIG}}(\tau-\delta) \cdot \Gamma_{\tilde{E}_{LO}}^*(\tau-\delta),
\end{aligned}$$

where the LO field is assumed to be stationary (unmodulated), whereas the signal field is cyclostationary with its time-dependent and lag-dependent (two-argument) ACF being periodic with a period equal to the symbol duration. After time averaging which involves omitting the time variable, it can be shown that  $\bar{\Gamma}_{\tilde{E}_{SIG}}(t-\delta, \tau)$ ,  $\bar{\Gamma}_{\tilde{E}_{SIG}}(t, \tau+\delta)$ , and  $\bar{\Gamma}_{\tilde{E}_{SIG}}(t-\delta, \tau-\delta)$  will finally lead to,  $\bar{\Gamma}_{\tilde{E}_{SIG}}(\tau+\delta)$  and  $\bar{\Gamma}_{\tilde{E}_{SIG}}(\tau-\delta)$ , respectively.

In Eq. (19), if we neglect the lineshape of the LO, i.e.  $S_{\tilde{E}_{LO}}(f) = 2P_{LO}\delta(f-\nu_{LO})$ , then  $\Gamma_{\tilde{E}_{LO}}(\tau) = 2P_{LO}$ . The reason for multiplying  $P_{LO}$  by 2 is that the total power of the complex envelope is twice that of the real field [29] since its respective ACF is given by  $\Gamma_{E_{LO}}(\tau) = \frac{1}{2} \text{Re} \left\{ \Gamma_{\tilde{E}_{LO}}(\tau) e^{j2\pi\nu\tau} \right\}$ . Now if we substitute for  $\Gamma_{\tilde{E}_{LO}}(\tau)$  in Eq. (19), we obtain

$$\begin{aligned}\bar{\Gamma}_{\Delta_{LO-SIG}}(\tau) = & P_{LO} \left( R_{SIG,s}^P R_{LO,s}^P + R_{SIG,s}^N R_{LO,s}^N \right) \cdot \text{Re} \left\{ \bar{\Gamma}_{\bar{E}_{SIG}}(\tau) e^{j2\pi\Delta\nu\tau} \right\} \\ & + P_{LO} \sqrt{R_{SIG,s}^P R_{LO,s}^P R_{SIG,s}^N R_{LO,s}^N} \cdot \left[ \text{Re} \left\{ \bar{\Gamma}_{\bar{E}_{SIG}}(\tau + \delta) e^{j2\pi\Delta\nu(\tau + \delta)} \right\} + \bar{\Gamma}_{\bar{E}_{SIG}}(\tau - \delta) e^{j2\pi\Delta\nu(\tau - \delta)} \right].\end{aligned}\quad (20)$$

Then, if we take the FT of ACF, we get the PSD of the LO-SIG term as

$$\begin{aligned}S_{\Delta_{LO-SIG}}(f) = & \text{FT} \left\{ \bar{\Gamma}_{\Delta_{LO-SIG}}(\tau) \right\} \\ = & P_{LO} \left[ \sqrt{R_{SIG,s}^P R_{LO,s}^P} + e^{j2\pi f\delta} \sqrt{R_{SIG,s}^N R_{LO,s}^N} \right]^2 \cdot \frac{1}{2} \left[ S_{\bar{E}_{SIG}}(f - \Delta\nu) + S_{\bar{E}_{SIG}}(-(f + \Delta\nu)) \right].\end{aligned}\quad (21)$$

In obtaining the expression in Eq. (21), we initially neglected the impulse responses of the  $P$  and  $N$  paths from the PD outputs up to current subtraction in the TIA which were denoted by  $h^P(t)$  and  $h^N(t)$ . It can be shown that the effects of those two impulse responses can be taken into consideration in the ACF of the LO-SIG as follows

$$\begin{aligned}\bar{\Gamma}_{\Delta_{LO-SIG}}(\tau) = & P_{LO} R_{SIG,s}^P R_{LO,s}^P \cdot \left( \text{Re} \left\{ \bar{\Gamma}_{\bar{E}_{SIG}}(\tau) e^{j2\pi\Delta\nu\tau} \right\} \otimes \Gamma_{h^P}(\tau) \right) + P_{LO} R_{SIG,s}^N R_{LO,s}^N \cdot \left( \text{Re} \left\{ \bar{\Gamma}_{\bar{E}_{SIG}}(\tau) e^{j2\pi\Delta\nu\tau} \right\} \otimes \Gamma_{h^N}(\tau) \right) \\ & + P_{LO} \sqrt{R_{SIG,s}^P R_{LO,s}^P R_{SIG,s}^N R_{LO,s}^N} \cdot \left( \text{Re} \left\{ \bar{\Gamma}_{\bar{E}_{SIG}}(\tau + \delta) e^{j2\pi\Delta\nu(\tau + \delta)} \right\} \otimes \Gamma_{h^P h^N}(\tau) \right) \\ & + P_{LO} \sqrt{R_{SIG,s}^P R_{LO,s}^P R_{SIG,s}^N R_{LO,s}^N} \cdot \left( \text{Re} \left\{ \bar{\Gamma}_{\bar{E}_{SIG}}(\tau - \delta) e^{j2\pi\Delta\nu(\tau - \delta)} \right\} \otimes \Gamma_{h^N h^P}(\tau) \right),\end{aligned}\quad (22)$$

where  $\Gamma_{h^P}(\tau)$ ,  $\Gamma_{h^N}(\tau)$ ,  $\Gamma_{h^P h^N}(\tau)$  and  $\Gamma_{h^N h^P}(\tau)$  are the deterministic ACFs and cross-correlations of the impulse responses  $h^P(t)$  and  $h^N(t)$  that can be calculated as follows

$$\begin{aligned}\Gamma_{h^P}(\tau) &= h^P(\tau) \otimes h^{P*}(-\tau), \quad \Gamma_{h^N}(\tau) = h^N(\tau) \otimes h^{N*}(-\tau), \\ \Gamma_{h^P h^N}(\tau) &= h^P(\tau) \otimes h^{N*}(-\tau), \quad \Gamma_{h^N h^P}(\tau) = h^N(\tau) \otimes h^{P*}(-\tau).\end{aligned}$$

Taking the FT of the ACF in Eq. (22) leads to the PSD of the LO-SIG beating term as

$$S_{\Delta_{LO-SIG}}(f) = P_{LO} \left[ H^P(f) \sqrt{R_{SIG,s}^P R_{LO,s}^P} + e^{j2\pi f\delta} H^N(f) \sqrt{R_{SIG,s}^N R_{LO,s}^N} \right]^2 \cdot \frac{1}{2} \left[ S_{\bar{E}_{SIG}}(f - \Delta\nu) + S_{\bar{E}_{SIG}}(-(f + \Delta\nu)) \right], \quad (23)$$

where  $H^P(f)$  and  $H^N(f)$  are the FT pairs of  $h^P(t)$  and  $h^N(t)$ , respectively.

Next, we evaluate the PSD of the received signal field  $S_{\bar{E}_{SIG}}(f)$ , which appears in Eq. (23). In fact, this PSD is related to the pulse shape and modulation format used at the transmitter. In fact, we can write the received signal field as

$$\tilde{E}_{SIG}(t) = \sum_{n=-\infty}^{\infty} (aX_n + bY_n)h(t - nT), \quad (24)$$

where  $h(t) = g(t) \otimes h_{CD}(t)$  is the overall impulse response including the transmitted pulse shape  $g(t)$  and CD impulse response  $h_{CD}(t)$ . Also,  $X_n$  and  $Y_n$  are the  $n^{\text{th}}$  information symbols on the two polarization states, i.e.  $X_n, Y_n \in \frac{1}{\sqrt{2}} \{ (1+j), (-1+j), (-1-j), (1-j) \}$  in the case of QPSK. In addition,  $a$  and  $b$  are the matrix entries of the  $2 \times 2$  Jones matrix ( $J$ ) representing the polarization rotation due to the misalignment between the state of polarization of the received signal and the axis of the CRx PBS, i.e.

$$J = \begin{bmatrix} a & b \\ -b^* & a^* \end{bmatrix}. \quad (25)$$

Using Eq. (24), we find the time averaged ACF of  $\tilde{E}_{SIG}(t)$ , denoted by  $\bar{\Gamma}_{\tilde{E}_{SIG}}(\tau)$ , as follows

$$\begin{aligned}\bar{\Gamma}_{\tilde{E}_{SIG}}(\tau) &= \overline{\langle \tilde{E}_{SIG}(t) \tilde{E}_{SIG}^*(t-\tau) \rangle} \\ &= |a|^2 \sum_{n=-\infty}^{\infty} \sum_{m=-\infty}^{\infty} \langle X_n X_m^* \rangle \overline{h(t-nT) h^*(t-\tau-mT)} + |b|^2 \sum_{n=-\infty}^{\infty} \sum_{m=-\infty}^{\infty} \langle Y_n Y_m^* \rangle \overline{h(t-nT) h^*(t-\tau-mT)} \\ &\quad + ab^* \sum_{n=-\infty}^{\infty} \sum_{m=-\infty}^{\infty} \langle X_n Y_m^* \rangle \overline{h(t-nT) h^*(t-\tau-mT)} + a^* b \sum_{n=-\infty}^{\infty} \sum_{m=-\infty}^{\infty} \langle X_n^* Y_m \rangle \overline{h(t-nT) h^*(t-\tau-mT)}.\end{aligned}\quad (26)$$

We know that for QPSK modulated symbols on the same polarization, we have

$$\langle X_n X_m^* \rangle = \langle Y_n Y_m^* \rangle = \begin{cases} 1 & n = m \\ 0 & n \neq m \end{cases},$$

and for independent QPSK symbols on different polarizations, we have

$$\langle X_n Y_m^* \rangle = \langle X_n^* Y_m \rangle = 0.$$

Hence, we can substitute with the statistical averages evaluated above into Eq. (26) to derive the ACF of the signal field as follows

$$\begin{aligned}\bar{\Gamma}_{\tilde{E}_{SIG}}(\tau) &= (|a|^2 + |b|^2) \sum_{n=-\infty}^{\infty} \overline{h(t-nT) h^*(t-\tau-nT)} \\ &= \frac{1}{T} \sum_{n=-\infty}^{\infty} \int_{-T/2}^{T/2} h(t-nT) h^*(t-\tau-nT) dt \\ &= \frac{1}{T} \int_{-\infty}^{\infty} h(t) h^*(t-\tau) dt \\ &= \frac{1}{T} \Gamma_h(\tau),\end{aligned}\quad (27)$$

where  $\Gamma_h(\tau) = \int_{-\infty}^{\infty} h(t) h^*(t-\tau) dt$  is the deterministic ACF of the overall pulse shape and

where we used the fact that  $|a|^2 + |b|^2 = 1$  since  $J$  is unitary. The integral in the second line of

Eq. (27) comes from the time averaging operator  $\overline{f(t)}$  being  $1/T \int_{-T/2}^{T/2} f(t) dt$  provided that

$f(t)$  is periodic with a period  $T$ . Hence, the PSD of the signal field  $S_{\tilde{E}_{SIG}}(f)$  required in Eq. (23) is given by the FT of the ACF as follows

$$S_{\tilde{E}_{SIG}}(f) = \frac{1}{T} |H(f)|^2 = \frac{1}{T} |G(f)|^2, \quad (28)$$

where  $H(f)$  and  $G(f)$  are the FT pairs of  $h(t)$  and  $g(t)$ , respectively. In the second equality of Eq. (28), we used the fact that  $|H_{CD}(f)|^2 = 1$ . Now if we back substitute in Eq. (23) after neglecting  $\Delta\nu$  (since it will be corrected in DSP afterwards) and integrate over frequency, we get the power of the desired LO-SIG photocurrent term (numerator of the SNR in Eq. (10))

$$\begin{aligned}
P_{\Delta_{LO-SIG}} &= P_{LO} \int_{-\infty}^{\infty} \left| H^P(f) \sqrt{R_{SIG,s}^P R_{LO,s}^P} + H^N(f) e^{j2\pi f \delta} \sqrt{R_{SIG,s}^N R_{LO,s}^N} \right|^2 \cdot \frac{1}{T} |G(f)|^2 |H_{rx-DSP}(f)|^2 df \\
&= \frac{2P_{LO} P_{SIG} \int_{-\infty}^{\infty} \left| H^P(f) \sqrt{R_{SIG,s}^P R_{LO,s}^P} + H^N(f) e^{j2\pi f \delta} \sqrt{R_{SIG,s}^N R_{LO,s}^N} \right|^2 |G(f)|^2 |H_{rx-DSP}(f)|^2 df}{\int_{-\infty}^{\infty} |G(f)|^2 df}, \quad (29)
\end{aligned}$$

where we employ the fact that the integral of the PSD of the complex envelope of the received signal field in Eq. (28) gives  $2P_{SIG}$ .

Regarding the LO-ON beating term, its ACF and PSD can be derived in a similar way as that used to obtain those quantities for the LO-ON term. In fact, the PSD of the LO-ASE beating will have a similar form to the one derived for the LO-SIG term which was given by Eq. (23), and can be expressed as

$$S_{\Delta_{LO-ON}}(f) = P_{LO} \left| H^P(f) \sqrt{R_{SIG,s}^P R_{LO,s}^P} + H^N(f) e^{j2\pi f \delta} \sqrt{R_{SIG,s}^N R_{LO,s}^N} \right|^2 \cdot \frac{1}{2} \left[ S_{\tilde{E}_{ON}}(f - \Delta\nu) + S_{\tilde{E}_{ON}}(-(f + \Delta\nu)) \right], \quad (30)$$

where  $S_{\tilde{E}_{ON}}(f)$  is the PSD of the complex envelope of the ASE field within one channel, which can be assumed as that of a narrowband filtered white noise given by

$$S_{\tilde{E}_{ON}}(f) = \begin{cases} 2N_o & |f| \leq B_{ch}/2 \\ 0 & |f| > B_{ch}/2 \end{cases}, \quad (31)$$

where  $N_o$  is the PSD level of the real-valued ASE noise field in W/Hz and  $B_{ch}$  is the optical bandwidth of one WDM channel. In Eq. (31), we made use of the assumption that the NL-induced noise portion inside  $\tilde{E}_{ON}$  can be assumed locally white, i.e. it has an approximately flat spectrum within one WDM channel [27]. Hence, the total optical noise field  $\tilde{E}_{ON}$  can be assumed white. Next, we can easily find the variance (or AC electrical power) of the LO-ON beating photocurrent term in the denominator of the SNR in Eq. (10) as follows

$$\sigma_{\Delta_{LO-ON}}^2 = \frac{2P_{LO} P_{ON} \int_{-B_{ch}/2}^{B_{ch}/2} \left| H^P(f) \sqrt{R_{SIG,s}^P R_{LO,s}^P} + H^N(f) e^{j2\pi f \delta} \sqrt{R_{SIG,s}^N R_{LO,s}^N} \right|^2 |H_{rx-DSP}(f)|^2 df}{B_{ch}}. \quad (32)$$

## 6.2 Derivation of ACF, PSD and power of the residual SIG-SIG beating term in the differential photocurrent

Similar to subsection 6.1 in this appendix, we begin by neglecting the effect of the impulse responses  $h^P(t)$ ,  $h^N(t)$  in Eq. (7) and later take them into consideration by modifying the final PSD expression obtained. We start by writing the definition of the time averaged ACF of  $\Delta i_{SIG-SIG}(t)$  obtained from the difference between the SIG-SIG beating terms in the  $P$  and  $N$  photocurrents in Eqs. (5) and (6), yielding

$$\begin{aligned}
\bar{\Gamma}_{\Delta_{SIG-SIG}}(\tau) &= \overline{\Delta i_{SIG-SIG}(t) \Delta i_{SIG-SIG}(t-\tau)} \\
&= \frac{1}{4} \left[ \sum_{i=1}^{N_{ch}} \sum_{j=1}^{N_{ch}} R_{SIG,i}^P R_{SIG,j}^P \overline{\left| \tilde{E}_{SIG,i}(t) \right|^2 \left| \tilde{E}_{SIG,j}(t-\tau) \right|^2} + \sum_{i=1}^{N_{ch}} \sum_{j=1}^{N_{ch}} R_{SIG,i}^N R_{SIG,j}^N \overline{\left| \tilde{E}_{SIG,i}(t-\delta) \right|^2 \left| \tilde{E}_{SIG,j}(t-\tau-\delta) \right|^2} \right] \\
&\quad - \sum_{i=1}^{N_{ch}} \sum_{j=1}^{N_{ch}} R_{SIG,i}^P R_{SIG,j}^N \overline{\left| \tilde{E}_{SIG,i}(t) \right|^2 \left| \tilde{E}_{SIG,j}(t-\tau-\delta) \right|^2} - \sum_{i=1}^{N_{ch}} \sum_{j=1}^{N_{ch}} R_{SIG,i}^N R_{SIG,j}^P \overline{\left| \tilde{E}_{SIG,i}(t-\delta) \right|^2 \left| \tilde{E}_{SIG,j}(t-\tau) \right|^2} \right].
\end{aligned}$$

In the above equation, all summation terms where  $i \neq j$  will involve the intensities of different channels which can be assumed independent, i.e. the expectation of the product can be evaluated as the product of expectations. Hence,

$$\begin{aligned}
\bar{\Gamma}_{\Delta_{\text{SIG-SIG}}}(\tau) &= \sum_{i=1}^{N_{\text{ch}}} \sum_{\substack{j=1 \\ j \neq i}}^{N_{\text{ch}}} (R_{\text{SIG},i}^P R_{\text{SIG},j}^P + R_{\text{SIG},i}^N R_{\text{SIG},j}^N - 2R_{\text{SIG},i}^P R_{\text{SIG},j}^N) P_{\text{SIG},i} P_{\text{SIG},j} \\
&\quad + \frac{1}{4} \sum_{i=1}^{N_{\text{ch}}} R_{\text{SIG},i}^P{}^2 \overline{\left\langle \left| \tilde{E}_{\text{SIG},i}(t) \right|^2 \left| \tilde{E}_{\text{SIG},i}(t-\tau) \right|^2 \right\rangle} + \frac{1}{4} \sum_{i=1}^{N_{\text{ch}}} R_{\text{SIG},i}^N{}^2 \overline{\left\langle \left| \tilde{E}_{\text{SIG},i}(t-\delta) \right|^2 \left| \tilde{E}_{\text{SIG},i}(t-\tau-\delta) \right|^2 \right\rangle} \\
&\quad - \frac{1}{4} \sum_{i=1}^{N_{\text{ch}}} R_{\text{SIG},i}^P R_{\text{SIG},i}^N \overline{\left\langle \left| \tilde{E}_{\text{SIG},i}(t) \right|^2 \left| \tilde{E}_{\text{SIG},i}(t-\tau-\delta) \right|^2 \right\rangle} - \frac{1}{4} \sum_{i=1}^{N_{\text{ch}}} R_{\text{SIG},i}^P R_{\text{SIG},i}^N \overline{\left\langle \left| \tilde{E}_{\text{SIG},i}(t-\delta) \right|^2 \left| \tilde{E}_{\text{SIG},i}(t-\tau) \right|^2 \right\rangle} \quad (33) \\
&= \sum_{i=1}^{N_{\text{ch}}} \sum_{\substack{j=1 \\ j \neq i}}^{N_{\text{ch}}} (R_{\text{SIG},i}^P R_{\text{SIG},j}^P + R_{\text{SIG},i}^N R_{\text{SIG},j}^N - 2R_{\text{SIG},i}^P R_{\text{SIG},j}^N) P_{\text{SIG},i} P_{\text{SIG},j} \\
&\quad + \frac{1}{4} \sum_{i=1}^{N_{\text{ch}}} R_{\text{SIG},i}^P{}^2 \bar{\Gamma}_{|\tilde{E}_{\text{SIG},i}|^2}(\tau) + \frac{1}{4} \sum_{i=1}^{N_{\text{ch}}} R_{\text{SIG},i}^N{}^2 \bar{\Gamma}_{|\tilde{E}_{\text{SIG},i}|^2}(\tau) \\
&\quad - \frac{1}{4} \sum_{i=1}^{N_{\text{ch}}} R_{\text{SIG},i}^P R_{\text{SIG},i}^N \bar{\Gamma}_{|\tilde{E}_{\text{SIG},i}|^2}(\tau+\delta) - \frac{1}{4} \sum_{i=1}^{N_{\text{ch}}} R_{\text{SIG},i}^P R_{\text{SIG},i}^N \bar{\Gamma}_{|\tilde{E}_{\text{SIG},i}|^2}(\tau-\delta),
\end{aligned}$$

where  $\bar{\Gamma}_{|\tilde{E}_{\text{SIG},i}|^2}(\tau)$  is the time averaged ACF of the squared envelope of the electric field of the  $i^{\text{th}}$  WDM signal which will be derived later. Then, the PSD of the SIG-SIG beating term in the differential photocurrent can be evaluated by taking the FT of its ACF given in Eq. (33) and written as

$$\begin{aligned}
S_{\Delta_{\text{SIG-SIG}}}(f) &= \delta(f) \sum_{i=1}^{N_{\text{ch}}} \sum_{\substack{j=1 \\ j \neq i}}^{N_{\text{ch}}} (R_{\text{SIG},i}^P R_{\text{SIG},j}^P + R_{\text{SIG},i}^N R_{\text{SIG},j}^N - 2R_{\text{SIG},i}^P R_{\text{SIG},j}^N) P_{\text{SIG},i} P_{\text{SIG},j} \\
&\quad + \frac{1}{4} \sum_{i=1}^{N_{\text{ch}}} \left| R_{\text{SIG},i}^P - e^{j2\pi f \delta} R_{\text{SIG},i}^N \right|^2 S_{|\tilde{E}_{\text{SIG},i}|^2}(f). \quad (34)
\end{aligned}$$

Now, we can take into consideration the impact of the impulse responses  $h^P(t)$  and  $h^N(t)$  in a way similar to that described prior to Eq. (23), which yields

$$\begin{aligned}
S_{\Delta_{\text{SIG-SIG}}}(f) &= \delta(f) \sum_{i=1}^{N_{\text{ch}}} \sum_{\substack{j=1 \\ j \neq i}}^{N_{\text{ch}}} (R_{\text{SIG},i}^P R_{\text{SIG},j}^P + R_{\text{SIG},i}^N R_{\text{SIG},j}^N - 2R_{\text{SIG},i}^P R_{\text{SIG},j}^N) P_{\text{SIG},i} P_{\text{SIG},j} \\
&\quad + \frac{1}{4} \sum_{i=1}^{N_{\text{ch}}} \left| H^P(f) R_{\text{SIG},i}^P - H^N(f) e^{j2\pi f \delta} R_{\text{SIG},i}^N \right|^2 S_{|\tilde{E}_{\text{SIG},i}|^2}(f), \quad (35)
\end{aligned}$$

where the first term in Eq. (35) represents a DC portion that is not of interest while calculating the residual SIG-SIG beat noise power  $\sigma_{\Delta_{\text{SIG-SIG}}}^2$  in Eq. (10). The second term in Eq. (35) represents the sum of the PSDs of the field intensities of all channels scaled by the quantity  $\left| H^P(f) R_{\text{SIG},i}^P - H^N(f) e^{j2\pi f \delta} R_{\text{SIG},i}^N \right|^2$  which represents the ability of the CRx to reject the common mode on both the  $P$  and  $N$  PDs. It is evident that this quantity is frequency dependent due to both the time skew and unequal frequency responses of the  $P$  and  $N$  paths.

Our next step is to derivethe PSD of the field intensity of one channel  $S_{|\tilde{E}_{\text{SIG},i}|^2}(f)$  required in Eq. (35). Without loss of generality, we will drop the subscript  $i$  and focus on the PSD of the squared envelope of one of the WDM channels  $S_{|\tilde{E}_{\text{SIG}}|^2}(f)$ . We begin by evaluating the

squared envelope of the received signal field given by Eq. (24) and then finding the time averaged ACF of the squared field envelope  $\bar{\Gamma}_{|\tilde{E}_{SIG}|^2}(\tau)$  as

$$\bar{\Gamma}_{|\tilde{E}_{SIG}|^2}(\tau) = \overline{\langle \tilde{E}_{SIG}(t) \tilde{E}_{SIG}^*(t) \tilde{E}_{SIG}(t-\tau) \tilde{E}_{SIG}^*(t-\tau) \rangle} \quad (36)$$

$$= \sum_{n=-\infty}^{\infty} \sum_{m=-\infty}^{\infty} \sum_{l=-\infty}^{\infty} \sum_{k=-\infty}^{\infty} \langle (aX_n + bY_n)(aX_m + bY_m)^*(aX_l + bY_l)(aX_k + bY_k)^* \rangle h(t-nT)h^*(t-mT)h(t-\tau-lT)h^*(t-\tau-kT),$$

where the statistical average of the product of four brackets can be evaluated as follows

$$\begin{aligned} \langle (aX_n + bY_n)(aX_m + bY_m)^*(aX_l + bY_l)(aX_k + bY_k)^* \rangle &= |a|^4 \langle X_n X_m^* X_l X_k^* \rangle + |b|^4 \langle Y_n Y_m^* Y_l Y_k^* \rangle \\ &\quad + |a|^2 |b|^2 \langle X_n X_m^* Y_l Y_k^* \rangle + |a|^2 |b|^2 \langle Y_n Y_m^* X_l X_k^* \rangle \\ &\quad + |a|^2 |b|^2 \langle Y_n X_m^* X_l Y_k^* \rangle + |a|^2 |b|^2 \langle X_n Y_m^* Y_l X_k^* \rangle \\ &\quad + \text{terms with vanishing statistical averages,} \end{aligned}$$

while noting that

$$\langle X_n X_m^* X_l X_k^* \rangle = \langle Y_n Y_m^* Y_l Y_k^* \rangle = \begin{cases} 1 & n = m \text{ \& } l = k \\ 1 & n = k \text{ \& } m = l \text{ \& } n \neq m, \\ 0 & \text{otherwise} \end{cases}$$

$$\langle X_n X_m^* Y_l Y_k^* \rangle = \langle Y_n Y_m^* X_l X_k^* \rangle = \begin{cases} 1 & n = m \text{ \& } l = k \\ 0 & \text{otherwise} \end{cases},$$

$$\langle Y_n X_m^* X_l Y_k^* \rangle = \langle X_n Y_m^* Y_l X_k^* \rangle = \begin{cases} 1 & n = k \text{ \& } l = m \\ 0 & \text{otherwise} \end{cases}.$$

Back substituting into Eq. (36) yields

$$\begin{aligned} \bar{\Gamma}_{|\tilde{E}_{SIG}|^2}(\tau) &= (|a|^4 + |b|^4) \cdot \left[ \sum_{n=-\infty}^{\infty} \sum_{l=-\infty}^{\infty} \overline{|h(t-nT)|^2 |h(t-\tau-lT)|^2} + \sum_{n=-\infty}^{\infty} \sum_{\substack{m=-\infty \\ n \neq m}}^{\infty} \overline{h(t-nT)h^*(t-mT)h(t-\tau-mT)h^*(t-\tau-nT)} \right] \\ &\quad + 2|a|^2 |b|^2 \left[ \sum_{n=-\infty}^{\infty} \sum_{l=-\infty}^{\infty} \overline{|h(t-nT)|^2 |h(t-\tau-lT)|^2} + \sum_{n=-\infty}^{\infty} \sum_{m=-\infty}^{\infty} \overline{h(t-nT)h^*(t-mT)h(t-\tau-mT)h^*(t-\tau-nT)} \right] \quad (37) \\ &= \frac{1}{T} (|a|^4 + |b|^4 + 2|a|^2 |b|^2) \sum_{l=-\infty}^{\infty} \Gamma_{|h|^2}(\tau-lT) + \frac{1}{T} (|a|^4 + |b|^4) \sum_{\substack{k=-\infty \\ k \neq 0}}^{\infty} C_h(\tau, k) + \frac{1}{T} 2|a|^2 |b|^2 \sum_{k=-\infty}^{\infty} C_h(\tau, k), \end{aligned}$$

where  $\Gamma_{|h|^2}(\tau) = \int_{-\infty}^{\infty} |h(t)|^2 |h(t-\tau)|^2 dt$  is the deterministic ACF of the squared envelope of

the overall pulse shape and  $C_h(\tau, k) = \int_{-\infty}^{\infty} h(t)h^*(t-\tau)h^*(t-kT)h(t-\tau-kT)dt$ . In order to

obtain the last line in Eq. (37), we perform some lengthy algebraic manipulations on the two double summations. The first double summation is manipulated as

$$\begin{aligned}
\sum_{n=-\infty}^{\infty} \sum_{l=-\infty}^{\infty} \overline{|h(t-nT)|^2 |h(t-\tau-lT)|^2} &= \frac{1}{T} \sum_{n=-\infty}^{\infty} \sum_{l=-\infty}^{\infty} \int_{-T/2}^{T/2} |h(t-nT)|^2 |h(t-\tau-lT)|^2 dt \\
&= \frac{1}{T} \sum_{n=-\infty}^{\infty} \int_{-T/2}^{T/2} |h(t-nT)|^2 \sum_{l=-\infty}^{\infty} |h(t-\tau-lT)|^2 dt, \text{ let } t-nT=z \\
&= \frac{1}{T} \sum_{n=-\infty}^{\infty} \int_{-nT-T/2}^{-nT+T/2} |h(z)|^2 \sum_{l=-\infty}^{\infty} |h(z-\tau-(l-n)T)|^2 dz \\
&= \frac{1}{T} \sum_{l=-\infty}^{\infty} \int_{-\infty}^{\infty} |h(z)|^2 |h(z-\tau-lT)|^2 dz \\
&= \frac{1}{T} \sum_{l=-\infty}^{\infty} \Gamma_{|h|^2}(\tau-lT), \quad \text{where } \Gamma_{|h|^2}(\tau) = \int_{-\infty}^{\infty} |h(t)|^2 |h(t-\tau)|^2 dt
\end{aligned}$$

and the second double summation is evaluated similarly as

$$\begin{aligned}
\sum_{\substack{n=-\infty \\ n \neq m}}^{\infty} \sum_{\substack{m=-\infty \\ m \neq n}}^{\infty} \overline{h(t-nT)h^*(t-mT)h(t-\tau-mT)h^*(t-\tau-nT)} &= \frac{1}{T} \sum_{n=-\infty}^{\infty} \sum_{\substack{m=-\infty \\ m \neq n}}^{\infty} \int_{-T/2}^{T/2} h(t-nT)h^*(t-mT)h(t-\tau-mT)h^*(t-\tau-nT) dt \\
&= \frac{1}{T} \sum_{n=-\infty}^{\infty} \int_{-T/2}^{T/2} h(t-nT)h^*(t-\tau-nT) \left[ \sum_{\substack{m=-\infty \\ m \neq n}}^{\infty} h^*(t-mT)h(t-\tau-mT) \right] dt, \text{ let } t-nT=z \\
&= \frac{1}{T} \sum_{n=-\infty}^{\infty} \int_{-nT-T/2}^{-nT+T/2} h(z)h^*(z-\tau) \left[ \sum_{\substack{m=-\infty \\ m \neq n}}^{\infty} h^*(z-(m-n)T)h(z-\tau-(m-n)T) \right] dz \\
&= \frac{1}{T} \sum_{\substack{k=-\infty \\ k \neq 0}}^{\infty} \int_{-\infty}^{\infty} h(t)h^*(t-\tau)h^*(t-kT)h(t-\tau-kT) dt \\
&= \frac{1}{T} \sum_{\substack{k=-\infty \\ k \neq 0}}^{\infty} C_h(\tau, k), \quad \text{where } C_h(\tau, k) = \int_{-\infty}^{\infty} h(t)h^*(t-\tau)h^*(t-kT)h(t-\tau-kT) dt
\end{aligned}$$

Next, applying the FT to the ACF obtained in Eq. (37) yields the desired PSD of the squared envelope (or intensity) of one channel  $S_{|\tilde{E}_{SIG}|^2}(f)$  on the form

$$\begin{aligned}
S_{|\tilde{E}_{SIG}|^2}(f) &= \frac{1}{T^2} \cdot \left| FT\{h(t)h^*(t)\} \right|^2 \sum_{l=-\infty}^{\infty} \delta\left(f - \frac{l}{T}\right) \\
&\quad + \frac{1}{T} \sum_{k=-\infty}^{\infty} \left| FT\{h(t)h^*(t-kT)\} \right|^2 - \frac{1}{T} (|a|^4 + |b|^4) \left| FT\{h(t)h^*(t)\} \right|^2 \\
&= \frac{1}{T^2} |H(f) \otimes H^*(-f)|^2 \sum_{l=-\infty}^{\infty} \delta\left(f - \frac{l}{T}\right) \\
&\quad + \frac{1}{T} \sum_{k=-\infty}^{\infty} |H(f) \otimes (e^{-j2\pi f k T} H^*(-f))|^2 - \frac{1}{T} (|a|^4 + |b|^4) |H(f) \otimes H^*(-f)|^2,
\end{aligned} \tag{38}$$

where in obtaining Eq. (38), we first proved and then employed the following FT pairs

$$FT\{\Gamma_{|h|^2}(\tau)\} = \left| FT\{h(t)h^*(t)\} \right|^2 = |H(f) \otimes H^*(-f)|^2,$$

$$FT\{C_h(\tau, k)\} = \left| FT\{h(t)h^*(t-kT)\} \right|^2 = |H(f) \otimes (e^{-j2\pi f k T} H^*(-f))|^2.$$

By carefully examining Eq. (38), we notice that the first term of  $S_{|\tilde{E}_{SIG}|^2}(f)$  is a summation of Dirac delta functions at discrete frequencies of  $l/T$  where  $l$  is an integer. The second and third terms represent the continuous portion of the PSD which depends on the pulse shape, residual CD and polarization orientation. Next, we make use of the derived PSD of the



intensity of one channel in Eq. (38) to evaluate the PSD of the residual SIG-SIG beating contribution in the differential photocurrent given by Eq. (35) while keeping only the relevant AC terms required for the SNR evaluation

$$S_{\Delta_{\text{SIG-SIG}}}^{AC}(f) = \frac{1}{4} \sum_{i=1}^{N_{ch}} \left| H^P(f) R_{\text{SIG},i}^P - H^N(f) e^{j2\pi f \delta} R_{\text{SIG},i}^N \right|^2 S_{|\tilde{E}_{\text{SIG},i}|^2}^{AC}(f), \quad (39)$$

where the PSD of the intensity of the  $i^{\text{th}}$  channel is written based on the form given by Eq. (38) in terms of the pulse shape and polarization orientation of the  $i^{\text{th}}$  channel as follows

$$S_{|\tilde{E}_{\text{SIG},i}|^2}^{AC}(f) = \frac{1}{T} \sum_{k=-\infty}^{\infty} \left| FT\{h_i(t)h_i^*(t-kT)\} \right|^2 - \frac{1}{T} (|a_i|^4 + |b_i|^4) \left| FT\{h_i(t)h_i^*(t)\} \right|^2, \quad (40)$$

where the subscripts  $i$  in Eq. (40) take into account the possibility of having different pulse shapes, CD and polarization orientation of different WDM channels. Finally if we integrate the PSD in Eq. (39) over frequency, we obtain the variance (AC power) of the residual SIG-SIG beating contribution in the differential photocurrent (required in Eq. (10) to evaluate the SNR) as follows

$$\begin{aligned} \sigma_{\Delta_{\text{SIG-SIG}}}^2 &= \frac{1}{4} \sum_{i=1}^{N_{ch}} \int_{-\infty}^{\infty} \left| H^P(f) R_{\text{SIG},i}^P - H^N(f) e^{j2\pi f \delta} R_{\text{SIG},i}^N \right|^2 S_{|\tilde{E}_{\text{SIG},i}|^2}^{AC}(f) |H_{\text{rx-DSP}}(f)|^2 df \\ &= \frac{1}{4} N_{ch} \sigma_{|\tilde{E}_{\text{SIG},se}|^2}^2 \frac{\int_{-\infty}^{\infty} \left| H^P(f) R_{\text{SIG}}^P - H^N(f) e^{j2\pi f \delta} R_{\text{SIG}}^N \right|^2 S_{|\tilde{E}_{\text{SIG}}|^2}^{AC}(f) |H_{\text{rx-DSP}}(f)|^2 df}{\int_{-\infty}^{\infty} S_{|\tilde{E}_{\text{SIG}}|^2}^{AC}(f) |H^{av}(f)|^2 |H_{\text{rx-DSP}}(f)|^2 df}, \end{aligned} \quad (41)$$

where in the second equality, we assumed the same responsivity for different WDM channels as well as equal intensity PSDs for various channels, i.e.  $S_{|\tilde{E}_{\text{SIG},i}|^2}^{AC}(f)$  is the same for any  $i$  which implies assuming the same CD, pulse shape and polarization orientation for different WDM channels [38]. Also,  $\sigma_{|\tilde{E}_{\text{SIG},se}|^2}^2 = \int_{-\infty}^{\infty} S_{|\tilde{E}_{\text{SIG}}|^2}^{AC}(f) |H^{av}(f)|^2 |H_{\text{rx-DSP}}(f)|^2 df$  is the variance

(or AC electrical power) of the photocurrent generated by the field intensity of one channel if detected with a single-ended PD having a unity responsivity and frequency response equal to the average frequency responses of the  $P$  and  $N$  PDs followed by DSP filtering. It is also

noticeable that  $\frac{1}{4} \sigma_{|\tilde{E}_{\text{SIG},se}|^2}^2 = \sigma_{|\tilde{E}_{\text{SIG}}|^2}^2$  because the power of the complex field is twice that of the real field. In addition, it can be shown that  $\sigma_{|\tilde{E}_{\text{SIG},se}|^2}^2 = \beta P_{\text{SIG}}^2$ , where  $\beta$  is a fractional scaling

factor defined as the ratio between the AC power of the filtered photocurrent generated by the field intensity of one channel and its DC electrical power (which is the squared DC power of the field itself assuming a unit responsivity). In fact,  $\beta$  was shown by simulations in [14] to be dependent on the residual CD and polarization orientation (see appendix B for further details on the scaling factor  $\beta$ ).

### 6.3 Power of the thermal and shot noise contributions in the photocurrent difference

Since shot noises generated from  $P$  and  $N$  PDs are uncorrelated, we can write the variance of their photocurrent difference  $\Delta i_{sh}(t) = i_{sh}^P(t) - i_{sh}^N(t)$  assuming, for simplicity, flat responsivity across the WDM spectrum and equal received signal powers for all WDM channels as follows

$$\sigma_{\Delta_{sh}}^2 = 2e \left[ (R_{LO}^N + R_{LO}^P) P_{LO} + N_{ch} (R_{\text{SIG}}^N + R_{\text{SIG}}^P) P_{\text{SIG}} \right] \Delta f \approx 4e \left[ R_{LO}^{av} P_{LO} + N_{ch} R_{\text{SIG}}^{av} P_{\text{SIG}} \right] \Delta f, \quad (42)$$

where  $\Delta f$  is the effective BW that depends on the overall frequency response of the receiver including PDs, TIAs, and DSP filtering as well as the transmitted pulse shape. In the second equality, we use the averaged LO and SIG responsivities over both the  $P$  and  $N$  PDs. Next, we also calculate the variance of the final photocurrent due to thermal noise as follows

$$\sigma_{\Delta i_{th}}^2 = (i_{TIA})^2 \Delta f, \quad (43)$$

where  $i_{TIA}$  is the input-referred noise current density which is an important specification for the TIAs, often provided in  $pA/\sqrt{Hz}$ .

#### 6.4 Expressions of PSDs of the LO-LO, SIG-ON and ON-ON beating contributions in the final differential photocurrent

Although we neglected the LO-LO, SIG-ON and ON-ON beating contributions when evaluating the PSD of the differential photocurrent in Eq. (9) since they were found negligible in our experiment, we present hereafter the final expressions of the PSDs of these three beat noise sources for the sake of completeness.

The PSDs of the differential photocurrents  $\Delta i_{LO-LO}(t)$ ,  $\Delta i_{SIG-ON}(t)$ , and  $\Delta i_{ON-ON}(t)$  can be obtained using the same procedure employed for other beating terms, that is by first evaluating the ACF of the photocurrent which, after a FT leads to the PSD. Below are the final expressions of the PSDs of the three beating contributions assuming the same responsivity for all WDM channels

$$S_{\Delta i_{LO-LO}}(f) = |H^P(f)R_{LO}^P - H^N(f)e^{j2\pi f\delta}R_{LO}^N|^2 \cdot P_{LO}^2 (\delta(f) + RIN(f)), \quad (44)$$

$$S_{\Delta i_{SIG-ON}}(f) = \frac{1}{4} |H^P(f)R_{SIG}^P - H^N(f)e^{j2\pi f\delta}R_{SIG}^N|^2 N_{ch} (S_{E_{SIG}}(f) \otimes S_{E_{ON}}(-f) + S_{E_{SIG}}(-f) \otimes S_{E_{ON}}(f)), \quad (45)$$

$$S_{\Delta i_{ON-ON}}(f) = |H^P(f)R_{SIG}^P - H^N(f)e^{j2\pi f\delta}R_{SIG}^N|^2 \left[ (N_o B_o)^2 \cdot \delta(f) + N_o^2 B_o \text{tri}\left(\frac{f}{B_o}\right) \right], \quad (46)$$

where  $RIN(f)$  is the spectrum of the relative intensity noise of the LO laser defined as

$$RIN(f) = \text{FT} \left\{ \langle \delta P_{LO}(t) \delta P_{LO}(t-\tau) \rangle / P_{LO}^2 \right\}, \quad (47)$$

where  $\delta P_{LO}(t)$  denotes the random intensity fluctuations of the LO laser optical power around its average power  $P_{LO}$ . Also, the triangular function in Eq. (46) is defined as

$$\text{tri}\left(\frac{f}{B_o}\right) = \begin{cases} 1 - \frac{|f|}{B_o} & |f| \leq B_o, \\ 0 & |f| > B_o \end{cases},$$

where  $B_o$  is the optical bandwidth of the WDM spectrum.

### 7. Appendix B: Dependence of the scaling factor of the SIG-SIG beating photocurrent on the residual CD and polarization orientation

In this appendix, we study in detail the scaling factor  $\beta$  presented in section 3. It is a fractional scaling factor equal to the ratio of the variance (or AC power) of the filtered photocurrent generated by the field intensity of one WDM channel relative to the DC electrical power of the photocurrent (which is the squared average optical power of the field itself assuming unit responsivity). In fact, it can be expressed as follows

$$\beta = \frac{\frac{1}{4} \int_{-\infty}^{\infty} S_{|\tilde{E}_{SIG}|^2}^{AC}(f) |H^{av}(f)|^2 |H_{rx-DSP}(f)|^2 df}{P_{SIG}^2}, \quad (48)$$

where  $S_{|\tilde{E}_{SIG}|^2}^{AC}(f)$  is the AC portion of the PSD of the intensity of the complex envelope of the signal field defined in Eq. (38),  $H^{av}(f)$  is the average frequency response of the  $P$  and  $N$  ports of the CRx,  $H_{rx-DSP}(f)$  is the frequency response representing all filtering performed at the receiver side DSP, and  $P_{SIG}$  is the average optical power of the field of one channel. By looking back at Eq. (38), we notice that  $S_{|\tilde{E}_{SIG}|^2}^{AC}(f)$  depends on the pulse shape and the residual CD (included in  $h(t)$ ) as well as on the polarization orientation of the received signal relative to the PBS axis of the CRx (represented by  $a$  and  $b$ ). Hence, the scaling factor  $\beta$  will in turn be dependent on the above parameters. In addition,  $\beta$  also tracks the overlap between the intensity spectrum  $S_{|\tilde{E}_{SIG}|^2}^{AC}(f)$  and the overall transfer function of the receiver side ( $H^{av}(f)$  and  $H_{rx-DSP}(f)$ ). In fact, the intensity spectrum is broader than the LO-SIG beating spectrum (desired term) which can be explained in view of Eq. (38) as follows:  $S_{|\tilde{E}_{SIG}|^2}^{AC}(f)$  is proportional to  $\sum_{k=-\infty}^{\infty} |H(f) \otimes (e^{-j2\pi f k T} H^*(-f))|^2$  meaning that the intensity spectrum is proportional to the squared magnitude of the convolution of the frequency response of the received field with phase shifted versions of itself and hence, the bandwidth of the intensity spectrum is expected to be double that of the received field. Thus, almost one half of the power of the intensity spectrum is rejected by filtering from the CRx itself and from the receiver DSP since this filtering is designated to pass only the desired signal spectrum.

In order to evaluate the impact of residual CD and polarization orientation on the scaling factor  $\beta$ , simulations are carried using a 28 Gbaud PDM-QPSK signal having  $10^5$  symbols. First, the symbols were pulse shaped using NRZ pulses at 16 samples/symbol. The NRZ pulse shape used in the simulation produces the QPSK intensity eyediagram shown in Fig. 13(a) which matches quite well the experimental intensity eyediagram obtained by direct detection after the single polarization IQ modulator (see Fig. 13(b)). After pulse shaping, the waveform was transmitted through various CD amounts ranging from 0 to 5 ns/nm. After CD was applied, the polarization of the waveform was rotated by some Jones angle ( $\theta$ ) by multiplying by the Jones matrix  $J$  defined in Eq. (25) where  $a = \cos(\theta)$  and  $b = \sin(\theta)$ , in order to simulate the misalignment between the state of polarization of the received signal and the axes of the CRx PBS. Then, the resulting waveform was convolved with the overall receiver's impulse response (assumed to be the matched filter in simulations). Finally, the variance (AC power) of the squared envelope (intensity) of the resulting filtered waveform is calculated and divided by its DC power resulting in the scaling factor  $\beta$ .

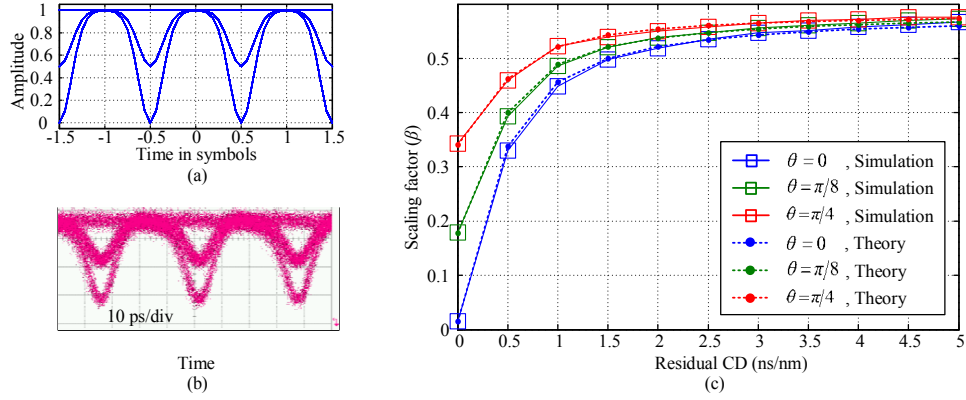


Fig. 13. (a) Simulated intensity eyediagram of the single polarization QPSK signal using NRZ pulse shape, (b) experimental intensity eyediagram obtained after the single polarization IQ modulator, (c) scaling factor ( $\beta$ ) versus the amount of residual CD for various polarization rotation angles ( $\theta$ ) obtained from simulations and theory on a 28 Gbaud PDM-QPSK signal.

Figure 13(c) plots  $\beta$  as evaluated from the simulation described above versus the amount of CD in ns/nm for various polarization rotation angles  $\theta$ . For the purpose of comparison, we also plot in Fig. 13(c)  $\beta$  versus the amount of CD at different polarization orientations as calculated from our theoretical expression in Eq. (48) with the application of Eq. (38) (derived in subsection 6.2) that expresses the PSD of the intensity in terms of the pulse shape, CD and polarization orientation. An excellent agreement is observed between the  $\beta$  values calculated from simulation and theory which verifies our analytical expressions. It is also noteworthy that the theoretical expressions derived can be employed to calculate  $\beta$  for any other pulse shape by plugging the impulse response of the pulse shape in Eq. (38) and then using Eq. (38) into Eq. (48). In addition,  $\beta$  can be evaluated for other modulation formats in a similar fashion to the one used for PDM-QPSK, however, a part of the derivation in subsection 6.2 has to be re-worked for the desired modulation format, specifically, the statistical average performed on the information symbols in Eq. (36), which was evaluated assuming PDM-QPSK modulation, has to be re-calculated for the new format.

Looking back to Fig. 13(c), we notice that the impact of the polarization orientation on  $\beta$  is significant for CD values less than 2 ns/nm (which corresponds to  $\sim 117$  km propagation over a fiber with dispersion parameter of 17 ps/(nm.km)). Within this CD range,  $\beta$  is at its maximum when  $\theta = \pi/4$  since for this polarization rotation angle, maximum crosstalk (and beating) between the two orthogonal polarizations of the received signal after passing through the PBS of the CRx results. Hence, this maximizes the peak-to-average ratio of the electrical signals at the output of the CRx which in turn increase the AC power of the photocurrent and finally increases  $\beta$ . On the other hand when the residual CD is larger than 2 ns/nm, the impact of  $\theta$  is less significant. In fact as the residual CD increases beyond 3 ns/nm,  $\beta$  increases until it saturates at a maximum value of around 0.55 regardless of polarization.

**Table 1. List of Symbols and Notation**

Notation	Explanation
$a$	Element in position (1,1) of the Jones matrix $J$
$b$	Element in position (1,2) of the Jones matrix $J$
$\beta$	Scaling factor representing the ratio between the AC electrical power of the photocurrent generated by the field intensity of one WDM channel relative to the DC electrical power of the photocurrent
$B_{ch}$	Optical bandwidth of one WDM channel
$CMRR_{SIG}$	Effective CMRR of the SIG-SIG beating
$\delta$	Time skew between the $P$ and $N$ paths
$\delta(f)$	Dirac delta function
$\delta P_{LO}(t)$	Random intensity fluctuations of the LO laser optical power
$\Delta i$	Total differential photocurrent
$\Delta i_{LO-SIG}$	Differential photocurrent due to LO beating with the signal
$\Delta i_{LO-ON}$	Differential photocurrent due to LO beating with incoming optical noise (ON)
$\Delta i_{SIG-SIG}$	Differential photocurrent due to residual SIG-SIG beating
$\Delta i_{ON-ON}$	Differential photocurrent due to ON-ON beating
$\Delta i_{SIG-ON}$	Differential photocurrent due to SIG-ON beating
$\Delta i_{LO-LO}$	Differential photocurrent due to LO-LO beating
$\Delta i_{sh}$	Differential photocurrent due to shot noise
$\Delta i_{th}$	Differential photocurrent due to thermal noise
$\Delta \nu$	Frequency offset between the LO and the WDM channel of interest (channel $s$ )
$e$	Electron charge
$E_{LO}$	Real-valued electric field of local oscillator laser
$E_{ON,i}$	Real-valued electric field of the total incoming optical noise for the $i^{\text{th}}$ WDM channel, including ASE and NL-induced noise
$E_{ON,s}$	Real-valued electric field of the total incoming optical noise for the $s^{\text{th}}$ WDM channel
$E_{SIG,i}$	Real-valued electric field of the signal for the $i^{\text{th}}$ WDM channel
$E_{SIG,s}$	Real-valued electric field of the signal for the $s^{\text{th}}$ WDM channel (assumed channel of interest)
$\tilde{E}_{SIG,i}$	Baseband complex envelope of the electric field of the signal for the $i^{\text{th}}$ WDM channel
$\tilde{E}_{ON,i}$	Baseband complex envelope of the electric field of the incoming optical noise for the $i^{\text{th}}$ WDM channel
$\tilde{E}_{LO}$	Baseband complex envelope of the electric field of the LO
FT $\{z\}$	Fourier transform of $z$
$\bar{\Gamma}_z(\tau)$	Time averaged autocorrelation function of $z$
$\Gamma_z(\tau)$	Autocorrelation function of $z$
$\Gamma_{z_1 z_2}(\tau)$	Cross-correlation function of $z_1$ and $z_2$
$G(f)$	Spectrum of transmitted pulse shape
$g(t)$	Impulse response of transmitted pulse shape
$H(f)$	Overall frequency response including transmitted pulse spectrum and the CD frequency response
$H^{av}(f)$	Average frequency response of the $P$ and $N$ ports of CRx, i.e. of $H^P(f)$ and $H^N(f)$
$h(t)$	Overall impulse response including the transmitted pulse shape and CD impulse response
$h^P(t)$	Impulse response of the path from $P$ PD up to current subtraction
$h^N(t)$	Impulse response of the path from $N$ PD up to current subtraction
$H_{CD}(f)$	Frequency response of CD
$h_{CD}(t)$	Impulse response of CD
$H^N(f)$	Frequency response of the path from $N$ PD up to current subtraction
$H^P(f)$	Frequency response of the path from $P$ PD up to current subtraction
$H_{rx-DSP}(f)$	Overall transfer function lumping all filtering within offline DSP

$i_{sh}^P$	Shot noise current at the $P$ photodiode
$i_{sh}^N$	Shot noise current at the $N$ photodiode
$i_{th}^P$	Input-referred thermal noise current at the $P$ photodiode
$i_{th}^N$	Input-referred thermal noise current at the $N$ photodiode
$i^N(t)$	Photocurrent at the output of $N$ photodiode
$i^P(t)$	Photocurrent at the output of $P$ photodiode
$i_{TIA}$	Input-referred noise current density of TIAs ( $A/\sqrt{Hz}$ )
$J$	$2 \times 2$ Jones matrix representing polarization rotation due to misalignment between state of polarization of the received signal and the CRx PBS
$\nu_{SIG,i}$	Optical frequency of the $i^{th}$ WDM signal
$\nu_{LO}$	Optical frequency of the LO
$N_{ch}$	Number of WDM channels incident on the receiver
$OSNR$	Optical signal-to-noise ratio
$P_{LO}$	Average LO power
$P_{NL}$	Average power of fiber nonlinearity-induced noise after dispersion unmanaged transmission
$P_{ON}$	Average power of the incoming optical noise measured at the CRx input
$P_{SIG}$	Average power of the received signal measured at CRx input
$P_z$	Average power of $z$
$R_{SIG,i}^P$	Effective responsivity at the wavelength of $i^{th}$ channel measured at the $P$ photodiode when light is applied to the SIG port
$R_{SIG,i}^N$	Effective responsivity at the wavelength of $i^{th}$ channel measured at the $N$ photodiode when light is applied to the SIG port
$R_{SIG,s}^P$	Effective responsivity at the channel of interest (channel $s$ ) measured at the $P$ photodiode when light is applied to the SIG port
$R_{SIG,s}^N$	Effective responsivity at the channel of interest (channel $s$ ) measured at the $N$ photodiode when light is applied to the SIG port
$R_{LO,s}^P$	Effective responsivity at the channel of interest (channel $s$ ) measured at the $P$ photodiode when light is applied to the LO port
$R_{LO,s}^N$	Effective responsivity at the channel of interest (channel $s$ ) measured at the $N$ photodiode when light is applied to the LO port
$\text{Re}\{z\}$	Real value of $z$
$RIN(f)$	Spectrum of laser's relative intensity noise (LO laser in our case)
$\sigma_z^2$	Variance (AC power) of $z$
$SNR$	Signal-to-noise ratio
$S_x(f)$	Power spectral density of $z$
$t$	Time variable
$T$	Symbol duration
$X_n$	$n^{th}$ transmitted symbol on X polarization
$Y_n$	$n^{th}$ transmitted symbol on Y polarization
$z^*$	Complex conjugate of $z$
$\langle z \rangle$	Statistical (ensemble) average of $z$
$\bar{z}$	Time average of $z$
$[z]^{AC}$	AC portion of $z$
$\otimes$	Convolution operator